J. Fluid Mech. (2011), *vol.* 667, *pp.* 96–134.
doi:10.1017/S0022112010004386

The mechanism of detonation attenuation by a porous medium and its subsequent re-initiation

MATEI I. RADULESCU† AND BRIAN McN. MAXWELL

Department of Mechanical Engineering, University of Ottawa, 161 Louis-Pasteur, Ottawa, ON, Canada K1N 6N5

(Received 14 September 2009; revised 12 August 2010; accepted 12 August 2010)

The attenuation and re-initiation mechanism of detonations transmitted through a porous section consisting of a two-dimensional array of staggered cylinders was investigated experimentally and numerically for acetylene–oxygen mixtures. It was found that the leading order attenuation mechanism is the wave diffraction around the cylinders. The local re-amplification permitting the self-propagation of the wave was due to wave reflections from adjacent obstacles. The critical conditions for transmittance of a detonation wave were found to correspond approximately to a pore size equal to approximately 30–60 detonation induction lengths, or one to two cell sizes. For quenched detonations, the re-initiation mechanism was found to rely on wave reflections from neighbouring pores. Depending on the mixture sensitivity, one or several shock reflections may be necessary to re-amplify the attenuated detonation wave back to a self-sustained wave. For the latter case, a novel mechanism was identified, where each shock reflection gives rise to a significant enhancement of the gas reactivity and burnout of large portions of unreacted gas. This leads to a slow acceleration of the leading front, punctuated by small-scale local sudden re-accelerations. The resulting wave interactions give rise to a topologically complex reaction zone structure consisting of alternating layers of reacted and unreacted gas. The role of turbulent diffusive burning during this transient is discussed.

Key words: detonation waves, gas dynamics, shock waves

1. Introduction

The propagation of a detonation wave through a porous medium is a fundamental multiscale detonation problem, whereby the local wave dynamics within the pores influence the global propagation characteristics of the wave. It is thus very similar to self-sustained unstable detonations, which have been shown to have hydrodynamic thicknesses a few orders of magnitude larger than the small-scale elements forming the reaction zone structure (Radulescu *et al.* 2007). In practice, the problem of detonation transmission through a porous medium has direct application to the design of detonation arrestors. Indeed, as a detonation wave travels through a porous medium, experiments indicate that a velocity deficit as high as 70 % of the ideal Chapman–Jouguet (CJ) velocity can be established (Makris 1993; Makris *et al.* 1993, 1995; Slungaard, Engebretsen & Sonju 2003). At such low velocities, adiabatic compression by the leading shock is believed to no longer provide the ignition mechanism in the deflagration wave. Instead, turbulent transport is believed to play an

† Email address for correspondence: matei@uottawa.ca

increasing role as dominating ignition mechanism, and strategies for flame arrestors involving heat losses and increase in the exposed surface area become efficient to further quench the reactions.

Experimentally, it is difficult to probe the flow-field details within the porous section. For this reason, the physical mechanism responsible for propagation of the detonations remains speculative. Makris performed a large series of experiments in a two-dimensional configuration permitting flow visualization, such that the flow fields can be monitored (Makris 1993). Open-shutter and schlieren photographs revealed some of the global characteristics of the flow field. Based on his observations, Makris proposed that wave reflections and turbulent mixing within each successive pore are responsible for maintaining the overall propagation. Nevertheless, the explanations were qualitative, and lacked analysis of the gas dynamic wave interactions to verify the conclusions made. A scaling was, however, proposed for the velocity-deficit dependence on the characteristic dimension of the pore size. Makris has found that his and several previous experiments can be re-scaled, such that an approximate velocity deficit of 50 % corresponds to a ratio between the characteristic pore dimension and cell size in the mixture of approximately 1 to 2. A similar scaling was also proposed by Dorofeev *et al.* (2000) based on an alternative definition of the characteristic length scale of the pore dimension.

A simplified one-dimensional porous medium was also considered as a sequence of chambers separated by narrow passages (Lyamin *et al.* 1991). They concluded from their experiments that the propagation mechanism can be viewed as a sequence of failures and re-initiations due to wave diffractions and re-initiations inside the successive chambers. These conclusions were very similar to the ones obtained by Teodorczyk, Lee & Knystautas (1988), who studied the propagation of so-called *quasi-detonations*, i.e. detonations with a high velocity deficit, in tubes with large periodic baffle plates positioned perpendicular to the flow direction. From their schlieren photographs, they also attributed the propagation mechanism to periodic re-ignitions from re-compression by the reflections of diffracting shocks. However, they point out that the experiments cannot discriminate between whether the ignition mechanism was from adiabatic compression or by turbulent mixing of shocked gases with combustion products, which may occur along the shear layers accompanying Mach reflections.

Although significant effort has been devoted to the detonations propagating through porous media, previous experimental studies did not address the detonation re-initiation mechanism following the attenuation by a porous medium. This problem is of course of prime importance to the design of detonation arrestors. Furthermore, Makris (1993) pointed out that the mechanism of re-initiation of a detonation after its interaction with one column of cylinders, involving diffraction and further reflections, can be instrumental in clarifying the mechanism of re-initiation in the porous medium itself. This re-initiation phase from one or several columns of cylinders is addressed in the present investigation.

The problem we study also bears similarity to the problem of detonation re-initiation after its interaction with a perforated plate, studied by Chao (2006) and Zhu, Chao & Lee (2007). In these studies, streak photographs indicated that a metastable wave propagating at approximately half the CJ velocity was established after the interaction with the porous plate, although its propagation mechanism remained unclear.

Limited modelling has been attempted of the attenuation of detonations by porous media and none has been attempted for the subsequent re-initiation phase. Previous modelling efforts (Ikeh 1981; Kauffman, Chuanjun & Nicholls 1982; Gu 1987; Gu,

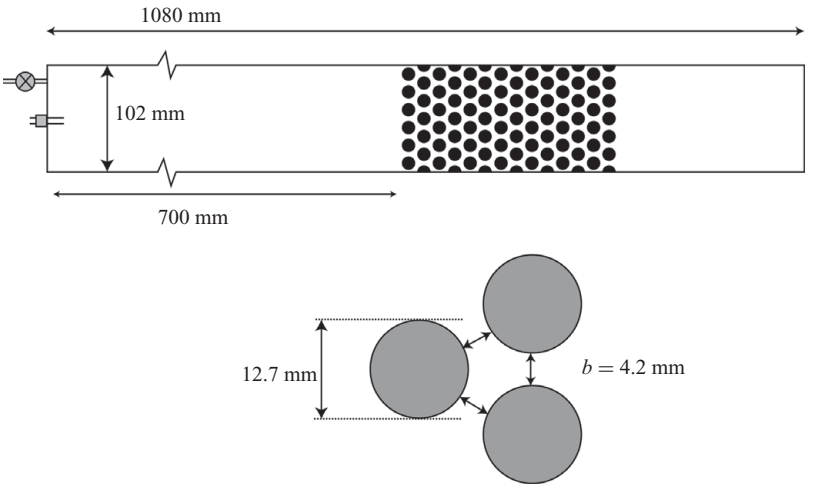

FIGURE 1. Experimental set-up.

Knystautas & Lee 1988; Frolov 1987; Zeldovich *et al.* 1987; Zhang & Lee 1994; Zhang *et al.* 1995; Dionne 2000; Dionne, Ng & Lee 2000; Brailovsky & Sivashinsky 2000, 2002; Bykov *et al.* 2004) were restricted to quasi-one-dimensional models pioneered by Zeldovich & Kompaneets (1960). These models account only for the propagation regimes by considering momentum and heat losses as volumetric source terms in the one-dimensional governing equations. Such models fail to relate the micro-physics to the global detonation propagation mechanism. Gamezo, Ogawa & Oran (2008) have attempted to clarify the propagation mechanism of detonations in geometries similar to the porous media. In their simulations of detonation formation in tubes with baffles, they identified different mechanisms for flame acceleration and propagation. However, these conclusions do not directly extend to the self-sustained regimes of propagation in dense porous media of the type studied here.

The present paper presents a series of experiments and numerical simulations aimed at clarifying the detonation propagation mechanism in a dense porous medium and its subsequent re-initiation. The simulations treat explicitly the coupling between non-steady two-dimensional gas dynamic interactions and their effect on the reaction rates within and at the exit of the porous medium. Such detailed simulations can offer significantly more insight over the quasi-one-dimensional models, and are aimed at clarifying the mechanism of detonation propagation and re-initiation following the detonation interaction with a porous medium observed in the experiments. This paper is organized as follows. Section 2 presents the experimental results of the detonation attenuation and its subsequent re-initiation following the interaction with a porous medium. Sections 3 and 4 present the numerical model used to investigate the mechanism of re-initiation of detonations following attenuation by a porous medium. These are followed by further discussions in § 5, suggesting future directions to address the outstanding issues.

2. Experiments

The experiments were conducted at the Shock Wave Physics Group Laboratory at McGill University. The experimental chamber was a 3 mm thin channel made of aluminium, approximately 100 mm in height and 1 m in length, as shown schematically in figure 1. The porous section consisted of 14 columns of 12.7 mm diameter PVC

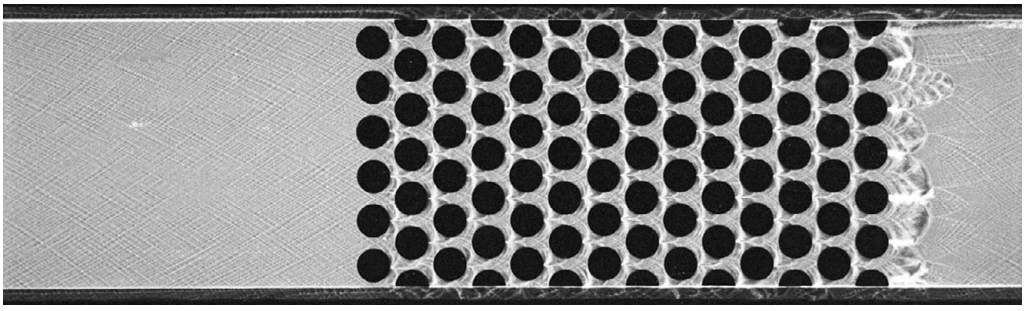

FIGURE 2. Open-shutter photograph of flow field at $p_o = 7.1\,\text{kPa}$.

cylinders, spaced in a uniform staggered distribution, shown to scale in figure 1. The spacing between the cylinders was 4.2 mm, denoted henceforth as the pore size, b. The entrance to the porous section was approximately 700 mm from the ignition point. One side of the channel was made of glass, in order to allow visualization of the flow field by open-shutter photography. The opposing wall was covered with a matte black paint, in order to avoid light reflection.

All experiments were performed using an equimolar mixture of acetylene (C_2H_2) and oxygen (O_2), prepared prior to the experiments by the method of partial pressures in a large vessel. The apparatus was flushed several times with the working mixture in order to eliminate any trace gases prior to its final fill at the desired pressure. In the experiments, the detonatable mixture sensitivity was controlled by the initial pressure, p_o. Initiation was achieved by a weak spark from an EG&G TM-11 trigger module. Detonations were rapidly formed by the use of a few obstacles placed near the ignition source. All experiments were monitored via open-shutter photography. Single photographs were recorded on 35 mm Kodak TMax 400 film with a 35 mm camera equipped with a 35 mm focal length lens. No other filtering equipment was used. In some experiments, two simultaneous open-shutter photographs were acquired to provide further resolution of the exit section.

Figure 2 shows the history of light emission obtained at an initial pressure of 7.1 kPa, while figure 3 shows a close-up of the same experiment near the exit of the porous section. The photographs illustrate the path of the triple points on the detonation structure as the detonation wave travels from left to right. On the left of the porous section in figure 2, the characteristic fish-scale pattern of a self-sustained detonation can be clearly observed. This cellular structure is periodically re-formed within the pores separating the cylinders.

For clarity, the various observed features are shown schematically in figure 4. The details of the open-shutter photographs show that the detonation wave is periodically re-initiated inside the porous section, as can be seen by the onset of new cellular structures. The features observed are very similar to those of Makris (1993) for porous sections with much higher porosity.

The interesting observation, however, pertains to the re-initiation of the detonation at the exit of the porous section, shown in figure 3. The enlargement of the cellular structures along the axis of the pores is consistent with previous observations of detonation diffraction (see e.g. Lee 2008). The enlargement and local disappearance of transverse bands is interpreted as detonation quenching due to diffraction of the wavefronts around each cylinder.

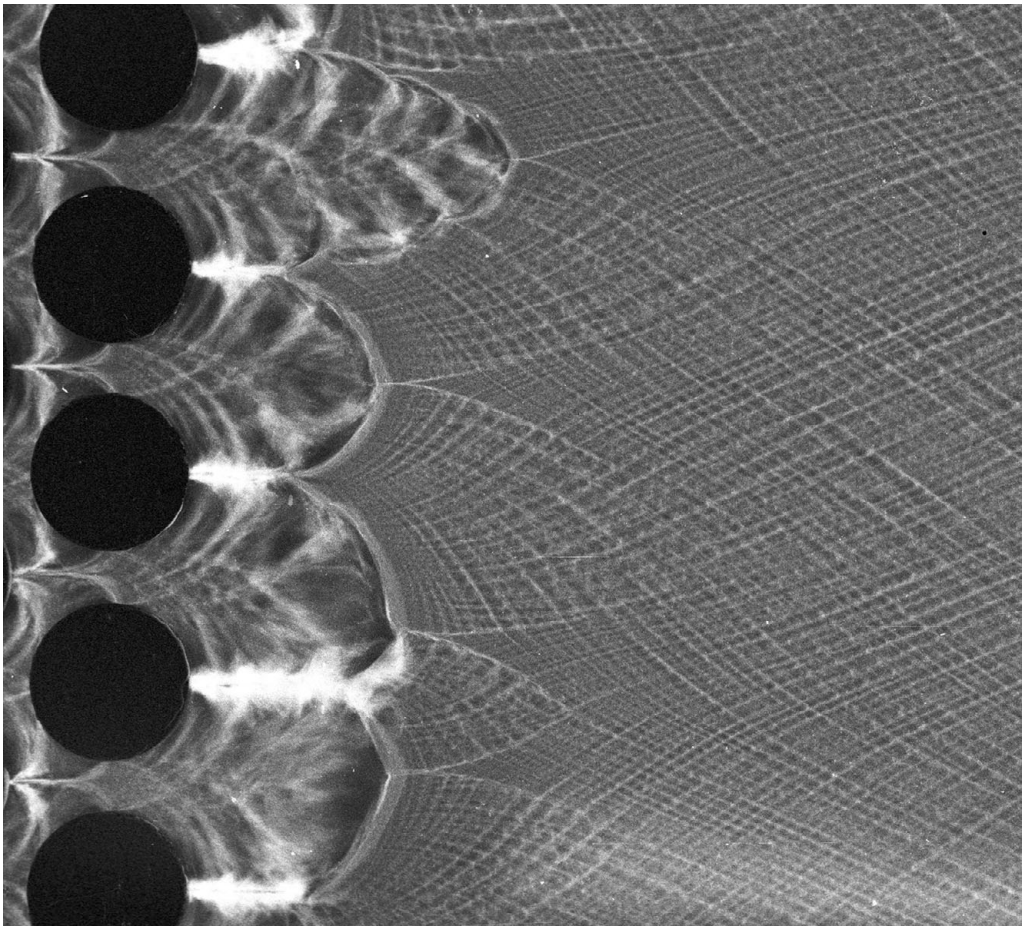

FIGURE 3. Detail of figure 2 illustrating the critical detonation transmission.

Also, as evident in figure 3, a cellular detonation was re-established on the right-hand side, indicated by the fine cellular structure traced out by the detonation triple points. The simplest way to identify where the detonation originated is to trace back the path of triple points towards the left in the regions of small cells. The regions of small cells correspond to the regions, where the detonations were overdriven, i.e. regions from which the detonations decelerate and become self-sustaining. Furthermore, the trajectory of the two families of triple points also serve to indicate the direction of the leading shock, which propagates such that the two wave families form equal angles with the normal of the detonation front (see figure 4). As can be clearly seen, the detonations originate near the wake of the last row of cylinders. The numerical simulations below confirmed that their re-initiation originates from wave collisions from neighbouring pores. This re-initiation flow field is similar to the flow field that was observed experimentally by Khasainov *et al.* (2005), Sorin *et al.* (2009), Ohyagi *et al.* (2002) and Obara *et al.* (2008) in detonation diffraction experiments.

Figure 3 also shows the presence of very bright bands separating zones with cellular structure from zones without cellular structure. These are indicated in the schematic shown in figure 4. Note that the trajectory of their propagation is parallel to the

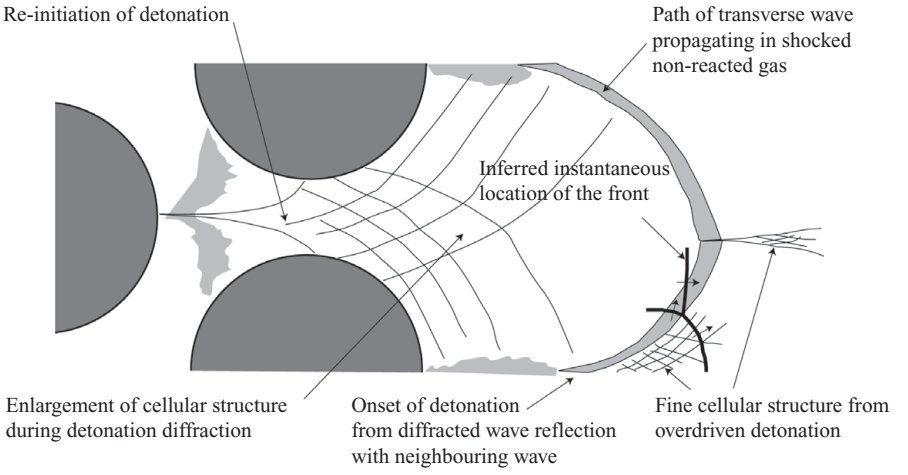

FIGURE 4. Sketch of the various features observed in the open-shutter photograph of figure 3.

trajectory of triple points in the detonation wave structure, suggesting that they are the path of triple points formed upon detonation initiation. This type of record has been previously investigated by Gamezo *et al.* (2000) and Pintgen & Shepherd (2009), who identified them as being transverse detonation waves propagating into shocked yet unreacted gas, also called 'super-detonations'. These waves are similar to the structure of the reflected (transverse) reactive wave in spinning detonations (Lee 2008).

Figure 3 illustrates the critical conditions for *direct* detonation transmission through the pores at a pressure of 7.1 kPa. For this pressure, the cell size is approximately 1.6 mm (Knystautas, Lee & Guirao 1982), yielding a critical ratio of pore size to cell size of 2.5. This criticality is well illustrated in figure 3 itself, where one can note that the upper pore shows successful detonation transmission along the pore axis, while the others do not, demonstrating the stochasticity near criticality. At pressures higher than 7 kPa, it was found that local detonation waves at each pore were able to transmit directly to the unconfined space on the right side, i.e. without the necessity of wave reflections from neighbouring pores. This is illustrated in figure 5, for a mixture at an initial pressure of 9 kPa. The figure clearly shows how a cellular detonation is periodically re-established in the porous section. At the exit of the last column of cylinders, the cellular detonation is not quenched, as the cellular structure is rapidly re-established.

At a pressure below 7 kPa, however, the re-initiation of the detonation wave downstream of the porous section becomes more complex. Figure 6 illustrates the integrated luminosity record obtained at 6 kPa. The interpretation of this open-shutter record is somewhat more difficult than above and will be explained by the numerical reconstruction given below. However, it can be immediately deduced that the re-initiation occurred first near the bottom of the photograph, since this is where a new cellular structure is observed closer to the cylinders, i.e. at the earliest time. Indeed, the orientation of the path of the triple points indicates that a detonation head near the bottom propagated upwards. There is also a re-initiation event near the top wall at a later time, as inferred by the growth of a cellular structure from that region.

The photograph also shows the presence of very distinct thick bright bands, originating immediately behind the cylinders where the first wave collisions took place.

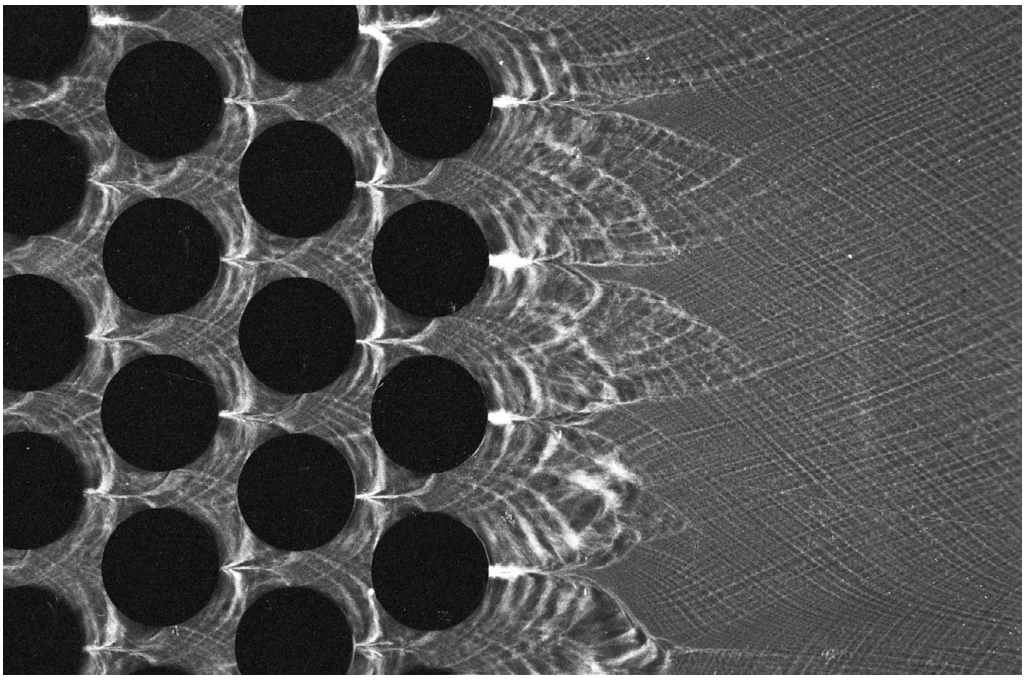

FIGURE 5. Open-shutter photograph of flow field at $p_o = 9$ kPa illustrating detonation transmission through the porous grid.

These bright bands do not correspond to super-detonations, since a cellular structure is absent, and their angle with the x-axis is smaller than if these waves propagated transversely at detonative speeds. In fact, following the numerical reconstruction below, these bands correspond more closely to the path of the triple points near the shock front. A likely explanation for the intense luminosity in these bands is the localized combustion events near the triple points. These are discussed in detail below, following the numerical reconstruction of the flow evolution in this critical regime.

Re-initiation from the coalescence of these bright bands, which we interpret as the location of triple point interactions, appeared to be the dominating mode of re-initiation at lower pressures, as illustrated in figure 7, obtained at 5 kPa. The cell size in this mixture is approximately 2.4 mm (Knystautas *et al.* 1982), yielding a ratio between the pore size and cell size of approximately 1.7. In figure 7, two detonation events can be identified. The first, towards the middle of the photograph, corresponds to the coalescence of two of these bright bands. The second, towards the bottom of the photograph, can be identified from the onset of a very fine cellular structure and transverse super-detonations.

At initial pressures below 4.5 kPa, re-initiation of detonations was not observed in our experiments. At pressures lower than 3 kPa, the deflagration wave was found to quench at the exit of the porous section. Figure 8 shows an open-shutter photograph obtained at 3 kPa, where re-initiation was not observed and the deflagration quenched, which is identified by the absence of luminosity at some locations on the right edge of the photograph. Figure 9 shows that as the pressure is further reduced, the deflagration wave quenches immediately at the exit of the porous section.

A further reduction of the pressure to 1.5 kPa, shown in figure 10, shows that the detonation wave in the upstream section becomes marginal, displaying the

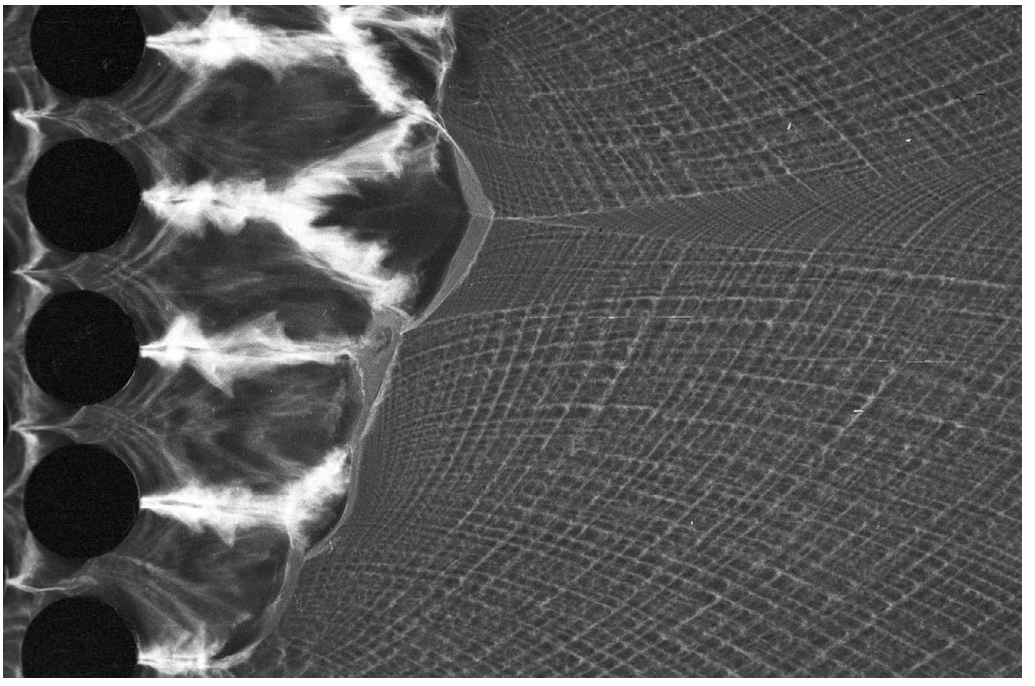

FIGURE 6. Open-shutter photograph of flow field at $p_o = 6\,\text{kPa}$.

characteristic sequence of failure and re-initiation accompanied by super-detonations (Gamezo *et al.* 2000). It is interesting to study the sequence of wave interactions at the left-hand side of the photograph with the four supporting cylinders and the subsequent dynamics of wave re-initiations via triple point reflections. Nevertheless, upon entrance of this marginal wave into the porous section, the entire wave is quenched after the sixth column of cylinders.

The marginal behaviour observed at lower pressures is likely due to the narrowness of the channel in comparison to the cell size, and the resulting boundary losses. At 1.5 kPa, the cell size is approximately 6 mm (Knystautas *et al.* 1982), such that the ratio of the channel thickness ($w = 3\,\text{mm}$) to the cell size is approximately 0.5. This limit is comparable with the result of previous investigations on the detonation limit in narrow channels. For example, Gamezo *et al.* (2000) find a similar marginal detonation wave in $C_2H_2 + 2.5O_2$ mixture at 3 kPa in a channel of 1.5 mm thickness. For this mixture, the cell size is approximately 5 mm (Knystautas *et al.* 1982), yielding a ratio of critical channel thickness to cell size of 0.3. In experiments of $C_2H_2 + 2.5O_2$, detonations propagating in a 0.05 mm thick channel, Manzhalei (1998) found the critical pressure for propagation to be 90 kPa. This corresponds to a cell size of 0.2 mm, and hence a ratio of the channel thickness to the cell size of also 0.3. Thus, this illustrates that when the cell size is larger than approximately two times the channel thickness, the detonation can no longer be self-sustained. This marginal behaviour can also be accounted for from first principles without any empirical input via boundary layer losses (Chao, Ng & Lee 2009).

This marginal behaviour is, however, interesting in its own right. It is interesting to note that the same bright bands observed at the exit of the porous wall section (e.g. in figures 6 and 7), are also observed intermittently in the marginal detonation of figure 10. In the latter, these can be associated unambiguously with the path

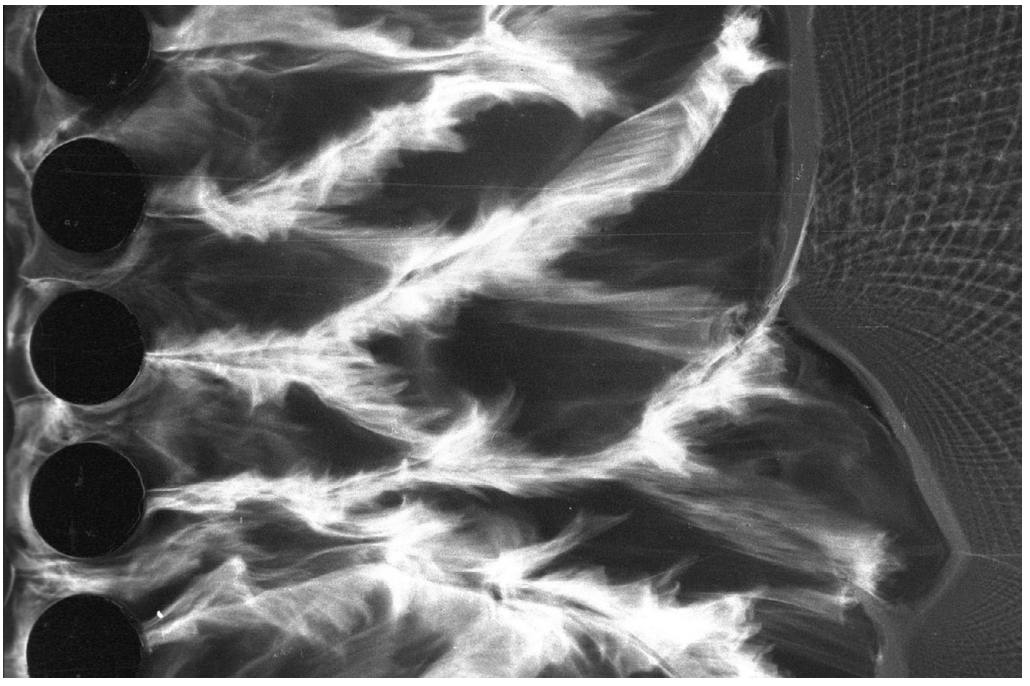

FIGURE 7. Open-shutter photograph of flow field at $p_o = 5\,\mathrm{kPa}$.

of attenuated triple point structures, similar to the observations of attenuated detonations in porous walled tubes (Radulescu & Lee 2002; Radulescu 2003). This gives further support to our interpretation of the flow field observed at the exit of the porous wall section.

3. The model

3.1. *Governing equations*

In this section, we aim to clarify the flow field inside the porous section and the mechanism for detonation re-establishment at its exit. To this effect, the detonation attenuation by the porous medium and its subsequent re-initiation is modelled by the two-dimensional reactive Euler equations for a perfect reacting gas with constant specific heats and molecular weight. For simplicity, we did not include any transport phenomena, i.e. neither the heat and viscous losses to boundary layers, nor the diffusion transport that can sustain flame propagation in diffusion dominated deflagrations. This restricts the model to fast gas dynamic and reactive phenomena, for which heat, mass and momentum diffusion are considered to operate on time scales much longer than the events modelled. This assumption will be carefully reviewed when comparing with the experiments in § 5.

The resulting conservation of mass, momentum and energy yield

$$\frac{\mathrm{D}\rho}{\mathrm{D}t} + \rho\nabla\cdot\boldsymbol{U} = 0, \tag{3.1}$$

$$\rho\frac{\mathrm{D}\boldsymbol{U}}{\mathrm{D}t} + \nabla p = 0, \tag{3.2}$$

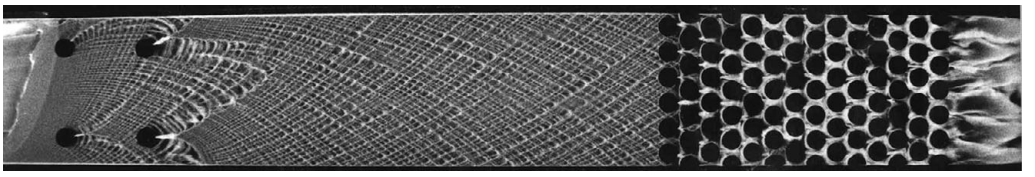

FIGURE 8. Open-shutter photograph of flow field at $p_o = 3\,\text{kPa}$.

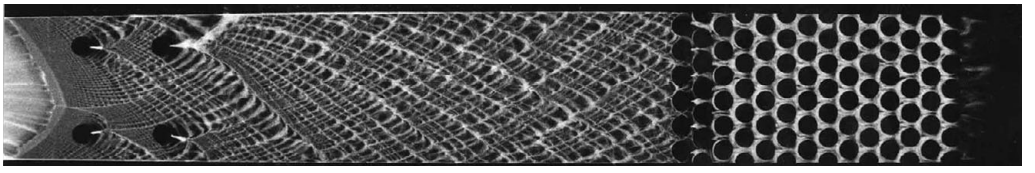

FIGURE 9. Open-shutter photograph of flow field at $p_o = 2\,\text{kPa}$.

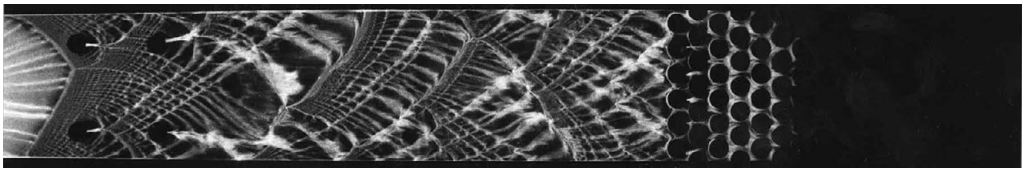

FIGURE 10. Open-shutter photograph of flow field at $p_o = 1.5\,\text{kPa}$.

$$\rho \frac{\mathrm{D}e}{\mathrm{D}t} = \frac{p}{\rho}\frac{\mathrm{D}\rho}{\mathrm{D}t} + \rho Q \frac{\mathrm{D}\alpha}{\mathrm{D}t}, \tag{3.3}$$

where $(\mathrm{D}/\mathrm{D}t)$ denotes the material derivative

$$\frac{\mathrm{D}}{\mathrm{D}t} \equiv \frac{\partial}{\partial t} + \boldsymbol{U}\cdot\nabla. \tag{3.4}$$

Here ρ is the density, p is the pressure, Q is the total energy release per unit mass and α is the progress variable of the chemical energy release; α takes a value of zero in the reactants and one in the products. The internal energy is written as

$$e = \frac{RT}{\gamma - 1}, \tag{3.5}$$

where γ is the isentropic index, an input in our model, defined as

$$\gamma \equiv \left(\frac{\partial \ln p}{\partial \ln \rho}\right)_s, \tag{3.6}$$

and the temperature satisfies the ideal gas law as follows:

$$T = \frac{p}{R\rho}, \tag{3.7}$$

where R is the specific gas constant.

3.2. *Thermal-kinetic model and parameters*

The input to our model is the isentropic index, the heat release and the dependence of the chemical-energy-release rate on the local thermodynamic state. These closure inputs were adjusted to model the equimolar acetylene–oxygen mixture at 5 kPa initial pressure and 300 K initial temperature.

Initial state	Composition	$C_2H_2 + O_2$
	Temperature	$T_o = 300\,\mathrm{K}$
	Pressure	$p_o = 5\,\mathrm{kPa}$
	Density	$\rho_o = 0.0582\ \mathrm{kg\,m^{-3}}$
Chapman–Jouguet solution	Detonation speed	$V_{CJ} = 2743\,\mathrm{m\,s^{-1}}$
	Detonation Mach number	$M_{CJ} = 8.23$
Von Neumann state	Density	$\rho_{VN} = 0.597\,\mathrm{kg\,m^{-3}}$
	Temperature	$T_{VN} = 2338\,\mathrm{K}$
	Isentropic exponent	$\gamma_{VN} = 1.16$
Kinetic properties	Ignition delay at constant volume	$\tau_i = 2.5 \times 10^{-7}\,\mathrm{s}$
	Global activation energy	$E_a/R = 10300\,\mathrm{K}$
	Half-reaction length	$\Delta_{1/2} \approx \tau_i u_{VN} = 0.067\,\mathrm{mm}$
	Cell size (Knystautas *et al.* 1982)	$\lambda = 2.4\,\mathrm{mm}$
Non-dimensional model parameters	Heat release	$Q/RT_o = 112\,(Q/RT_{VN} = 18)$
	Activation energy	$E_a/RT_o = 28\,(E_a/RT_{VN} = 4.4)$
	Isentropic exponent	$\gamma = 1.16$

TABLE 1. Thermo-chemical mixture properties and model parameters.

The heat release and isentropic index were evaluated using the NASA chemical equilibrium package CEA (Gordon & MCBride 1994). Chapman–Jouguet detonation calculations provided the detonation properties of the mixture, which are listed in table 1. The calculated Von Neumann (VN) state behind the leading shock propagating at CJ speed, assuming vibrational equilibrium and frozen chemistry, is also listed in table 1.

The isentropic exponent of our model was taken at the VN state found in the calculations, since the model is to capture the correct compressibility of the gases behind the shock. The global heat release Q was determined in order to reproduce the correct CJ Mach number, given for a perfect gas (Lee 2008) by

$$\frac{Q}{RT_o} = \frac{\gamma}{2(\gamma^2 - 1)}\left(M_{CJ} - \frac{1}{M_{CJ}}\right)^2. \tag{3.8}$$

For reference, this parameter is also listed in table 1 in terms of the VN temperature obtained in our model, given by the Rankine–Hugoniot shock jump conditions in a perfect gas

$$\frac{T_{VN}}{T_o} = 1 + \frac{2(\gamma - 1)\left(\gamma M_{CJ}^2 + 1\right)\left(M_{CJ}^2 - 1\right)}{M_{CJ}^2(\gamma + 1)^2}. \tag{3.9}$$

For simplicity, the rate of energy release is modelled by a first-order one-step reaction with Arrhenius dependence on temperature, yielding

$$\frac{\mathrm{D}\alpha}{\mathrm{D}t} = k(\alpha - 1)\mathrm{e}^{-E_a/RT}. \tag{3.10}$$

The global activation energy was determined from chemical kinetic calculations using the Sandiego thermal-kinetic database (Varatharajan & Williams 2001). Constant volume ignition calculations with the reactant gas initially at the VN state were conducted with the Cantera package (Goodwin 2010). Since the ignition delay for large activation energy is given to leading order by

$$\tau_i \propto \mathrm{e}^{E_a/RT}, \tag{3.11}$$

perturbations of the VN temperature by $\pm 10\,\%$ permitted an estimation of the activation energy from

$$\frac{E_a}{RT_{VN}} \approx \left| \frac{\partial \ln \tau_i}{\partial \ln T_{VN}} \right| \approx \left| \frac{\Delta \ln \tau_i}{\Delta \ln T_{VN}} \right|. \tag{3.12}$$

The resulting thermal kinetic parameters of our model are thus

$$\frac{E_a}{RT_{VN}} = 4.4, \quad \frac{Q}{RT_{VN}} = 18, \quad \gamma = 1.16. \tag{3.13}$$

The pre-exponential factor k was set to $k = 16.69979$ for all calculations such that the half-reaction length, $\Delta_{1/2}$, corresponding to the distance from the shock in the steady one-dimensional detonation solution to the point where half of the heat is released, corresponds to unity distance. This means that distances are normalized by $\Delta_{1/2}$. The results below are presented in non-dimensional form, using the initial pressure p_o as pressure scale, ρ_o as density scale and correspondingly $\sqrt{p_o/\rho_o}$ as velocity scale. For reference, the resulting time scale is thus $\Delta_{1/2}/\sqrt{p_o/\rho_o}$.

To recover the dimensional flow field and compare with experiment, one thus needs to prescribe the initial pressure, p_o, the initial density, ρ_o, and the dimensional half-reaction length, $\Delta_{1/2}$. These parameters are given in table 1 for the experiments conducted at $p_o = 5\,\mathrm{kPa}$. Note that the dimensional value of $\Delta_{1/2}$ was estimated by the induction length in the detonation reaction zone structure obtained with realistic chemistry, approximated by the product of the ignition delay at constant volume, τ_i, calculated with the full chemistry at the VN condition and the particle speed at the VN condition. Since the experiments were conducted by varying the initial pressure while keeping the initial temperature constant, the changes in ρ_o and $\Delta_{1/2}$ can be obtained, respectively, from the ideal gas law (3.7) and the real chemistry dependence of the induction length or cell size on the initial pressure, given approximately by $\Delta_{1/2} \propto \lambda_i \propto p_o^{-1.2}$ (Radulescu 2003).

3.3. *Computational domain, initial and boundary conditions*

A complete simulation of the experimental set-up would be computationally prohibitive. Choosing only one row of cylinders appears justified by the experimental observation that the flow field is similar in successive pores after each column of cylinders. Calculations with two and three columns of cylinders are also presented below for comparison. It was further assumed that the flow is perfectly reproducible from pore to pore in a single column of cylinders. Hence we made use of this symmetry and focused only on one half-cylinder. An example of the computational domain is given in figure 11.

Reflective boundary conditions were used on the top and bottom surfaces to denote the symmetry condition. To handle the curved geometry of the cylinders on the Cartesian grid used, we made use of the level set technique developed by Xu, Aslam & Stewart (1997) for internal solid boundaries.

The solution was initialized with the one-dimensional Zeldovich–Von Neuman–Doering (ZND) model (Lee 2008). The position of the ZND wave was placed before the first cylinder. The left boundary in the simulations is fixed with the CJ solution. In all cases, the simulation is stopped before any wave reaches either the left or right boundaries, which are placed sufficiently far from the cylinder.

We chose to initiate our calculations with the ZND solution, as opposed to a fully developed cellular detonation for two reasons. First, as will be demonstrated below, the large disturbances introduced by the interaction of the detonation with a cylinder

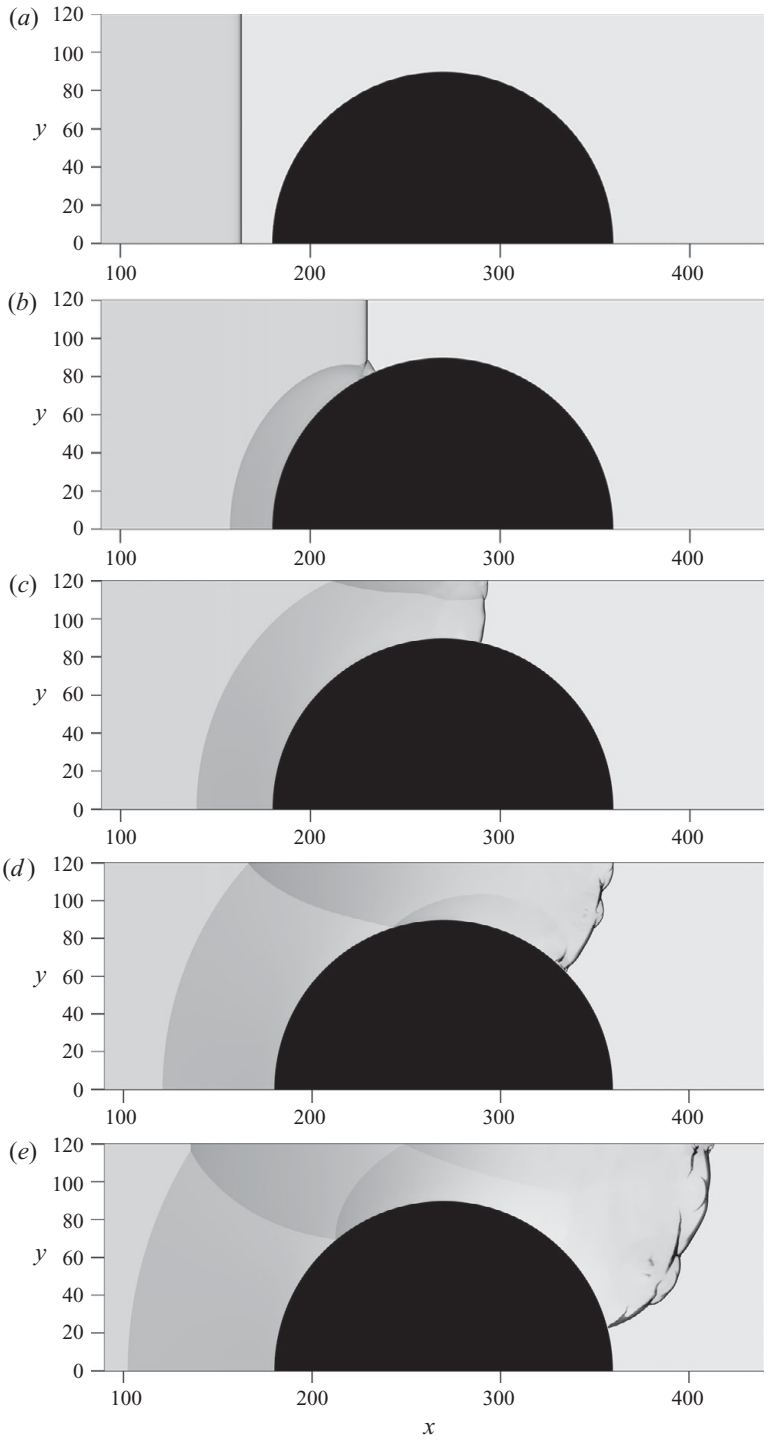

FIGURE 11. (*a–e*) For caption see facing page.

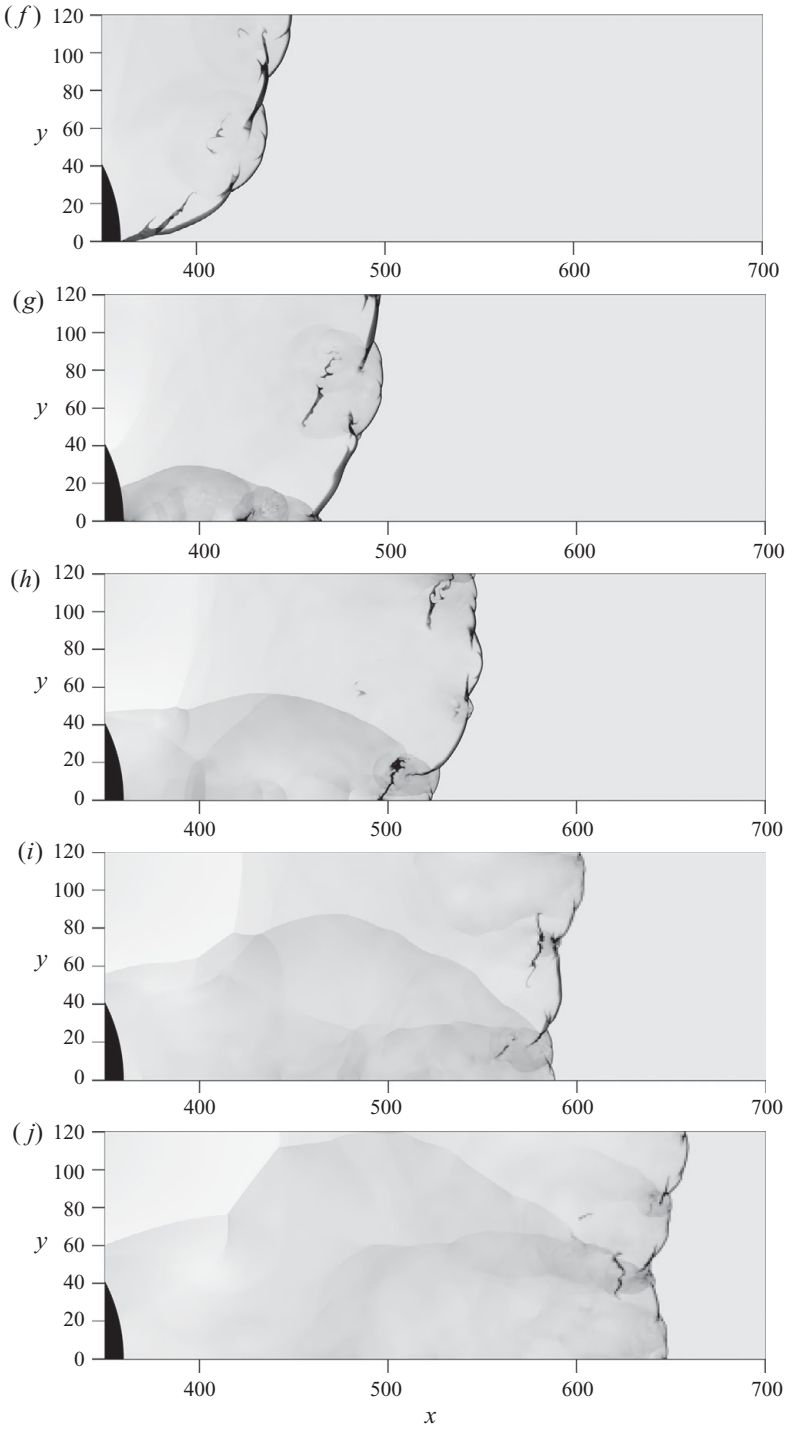

FIGURE 11. Density field evolution illustrating the detonation transmission for a non-dimensional pore size of $b = 60$; $(a–j)$ at $t = 0, 7.48, 14.0, 21.6, 29.4, 34.5, 41.8, 48.5, 54.6$ and 60.9; greyscale ranging from 0 to 1 given by $(\rho - 1)/9$.

and the following reflections are much larger than the disturbances induced by cellular pulsations of the front. This choice is also justified in hindsight (see below), since the outcome of a detonation wave interaction with a single cylinder, two cylinders or three cylinders is very similar, hence suggesting that the local perturbations set by the first cylinder do not affect the flow-field set by subsequent cylinders. Secondly, this choice of initial condition permitted us to unravel the complex flow-field set by the detonation interaction with the cylinders in detail; this would have been obscured by a pre-established cellular structure, hence making the numerical reconstruction more difficult to study. This technique was also used by Arienti & Shepherd (2005) to study the detonation diffraction problem.

3.4. *Numerical framework*

The numerical model detailed above was solved using the AMRITA software development system, developed by J. J. Quirk (Quirk 1998*a*,*b*). The Roe Riemann solver was used along with the *min–mod* slope limiter (Laney 1998). An adaptive mesh-refinement technique was used to obtain sufficient grid resolution to capture the reactivity field behind the leading interacting shocks. The base grid spacing corresponded to one $\Delta_{1/2}$. The finest grid consisted of 32 grid points per $\Delta_{1/2}$ of the ZND wave. Throughout the computations, the entire reaction zone was always covered by the finest grid. Other grid refinement criteria were chosen to ensure proper resolution of rapidly changing flow features and spatial gradients such as shock waves. This resolution was shown to be sufficient to capture transient detonation phenomena (Sharpe 2001). A grid convergence study is presented below.

4. Numerical results

4.1. *Re-initiation from the interaction with one cylinder*

4.1.1. $b = 60$

The interaction of a detonation wave with a cylinder for a pore size equal to 60 times $\Delta_{1/2}$, i.e. $b = 60$, is shown in figure 11. Recall that the pore size refers to the distance between adjacent cylinders, so in figure 11, the distance between the cylinder and the top boundary is $30\Delta_{1/2}$. The density field, as shown in figure 11, was chosen because it illustrates quite well the reaction-zone-structure evolution and the various shock and expansion waves. Figure 11(*a*) illustrates the initial planar ZND wave, in which the shocked and non-reacted gas prior to its ignition has a much higher density and appears dark in the record. In figure 11(*b–j*), the dark regions always correspond to shocked un-reacted gases.

Figure 11(*b*) illustrates the reflection of the ZND detonation on the cylinder surface and the resulting reflected wave into the burned gases. The reflection is a Mach reflection, similar to the one that was observed in the detonations interaction with cylinders in the experiments by Akbar (1997). In figure 11(*c*), the reflected wave reflected again on the top boundary and generated a new triple point. The shock near the top wall is now the new Mach stem, with an increase in strength.

The evolution of the strength of the front and the resulting reactivity of the gas behind the shocks can be seen in figures 12 and 13. Figure 12 shows the Mach number of the lead shock measured along the top boundary, while figure 13 shows the equivalent open-shutter photograph obtained numerically. This latter record was

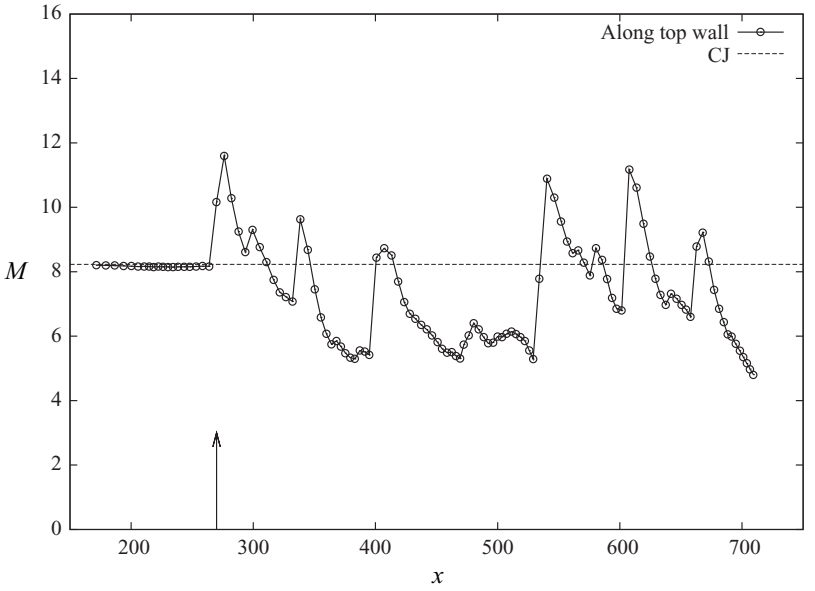

FIGURE 12. Shock Mach number recorded along the top boundary for a pore size of $b = 60$; the arrow indicates the position of the throat.

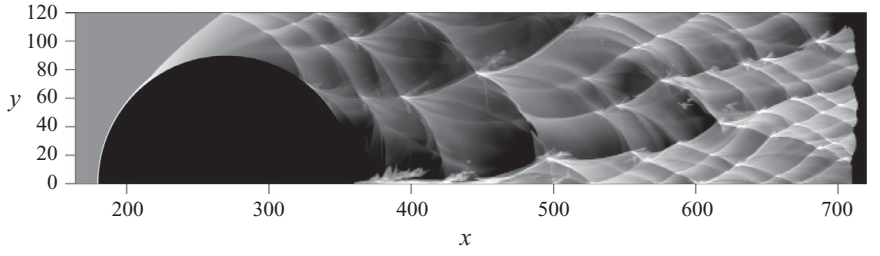

FIGURE 13. Maximum exothermicity field ξ for $b = 60$; greyscale ranging from 0 to 1 given by $(\log \xi + 0.7)/2$.

obtained by recording the maximum rate of energy release at every position (x, y)

$$\xi(x, y) = \mathrm{Max}\left(\rho \frac{\mathrm{D}\alpha}{\mathrm{D}t}\right) = \mathrm{Max}\left(k\rho(\alpha - 1)\mathrm{e}^{-\rho E_a/p}\right), \tag{4.1}$$

that was ever experienced at that particular location throughout the entire simulation. For reference, the logarithmic greyscale extends from a rate of energy release of an order of magnitude smaller than the peak energy release rate in a ZND wave (black) to an order of magnitude larger (white). Hence, this provided an unambiguous record of where the combustion rates are either amplified or slowed down. Figures 12 and 13 illustrate that the increase in reactivity during the propagation of the detonation in the converging area is indeed due to the successive reflections with the wall or with the cylinder's surface, which give rise to larger local shock Mach numbers.

Figure 11(*d*,*e*) also illustrates that following the two initial reflections, there are new triple points formed on the detonation structure via the wave bifurcation mechanism described in Radulescu *et al.* (2009) and Mach & Radulescu (2010). These new

triple points are also clearly visible in figure 13 as boundaries between gases of high exothermicity and gases with low exothermicity.

For the present conditions, the detonation remains self-sustained on the back side of the obstacle, as illustrated in figure 11(*f*–*i*). A global thickening of the reaction zone structure is, however, evident, accompanied by the formation of larger unreacted pockets, by the same mechanism as explained in Radulescu *et al.* (2007). The attenuation of the reaction rates behind the diffracting detonation is best seen in figures 12 and 13. Figure 12 shows a decay of the leading shock by approximately 25 % of the ideal CJ speed, while figure 13 shows that intermittent regions of high exothermicity persist only following triple shock interactions on the detonation wavefront. Figure 13 also shows the amplification of the reaction rates following the reflection of the diffracting front with the bottom boundary. For the present conditions, however, the detonation recovers from the diffraction process along the axis of the throat before any further compression waves arrive from the reflection event on the bottom wall (see figure 11); these are transmitted along the path of the triple points, which have not yet reached the axis as shown in figure 11(*j*). Along the axis of the throat, the wave thus rapidly recovers an average Mach number close to the Chapman–Jouguet value by self-acceleration, as indicated in figure 12. The dynamics illustrated in these numerical experiments are similar to the flow fields observed in figure 5.

4.1.2. $b = 30$

The equivalent effect of lowering the pressure in the experiments is to keep the same mixture parameters, and to decrease the dimension of the obstacles and channel width. In the numerical experiments, when the pore size is reduced by a factor of two to $b = 30$, the influence of the half-cylinder is to locally de-couple the shock and reaction zone in the detonation wave during the diffraction process. The evolution of the reaction zone during the diffraction transient is shown in figure 14, while figure 15 shows the time integrated maximum exothermicity plot. Owing to the shorter characteristic time for the diffraction process, as compared to the characteristic time of reaction in the un-attenuated detonation (which is kept constant here), the rapid rate of cooling during the diffraction process has a stronger effect on the reactions occurring behind the decaying shock. Consistent with the results of Eckett, Quirk & Shepherd (2000), Arienti & Shepherd (2005) and Radulescu & Maxwell (2010) for the quenching of the reactions during diffraction due to the gas dynamic cooling, we observe a thickening of the reaction zone structure and failure of the detonation to re-amplify along the axis of the pore. Figure 15 also indicates that the rate of energy release drops by more than an order of magnitude during this transient. We were not able to verify whether the reactions are fully quenched by unsteadiness, as was performed in Arienti & Shepherd (2005), since reactions always persist on contact surfaces due to numerical diffusion (see below). Nevertheless, it can be simply seen that the gases accumulating behind the decaying shock remain unreacted for the entire time of the simulation as a growing tongue-like structure, even after the detonation re-establishment from shock reflections.

When the detonation is not re-established along the pore axis, we refer to this event as a subcritical case of direct transmission of the detonation wave through the array of cylinders. However, the re-initiation of a detonation wave is still possible, as shown in figures 14 and 15. In this case, the initiation occurs following the reflection of the diffracted shock with the bottom boundary. This gives rise to a new Mach shock, which can clearly be seen in figure 14(*e*). Figure 14(*f*,*g*) shows that the reactant

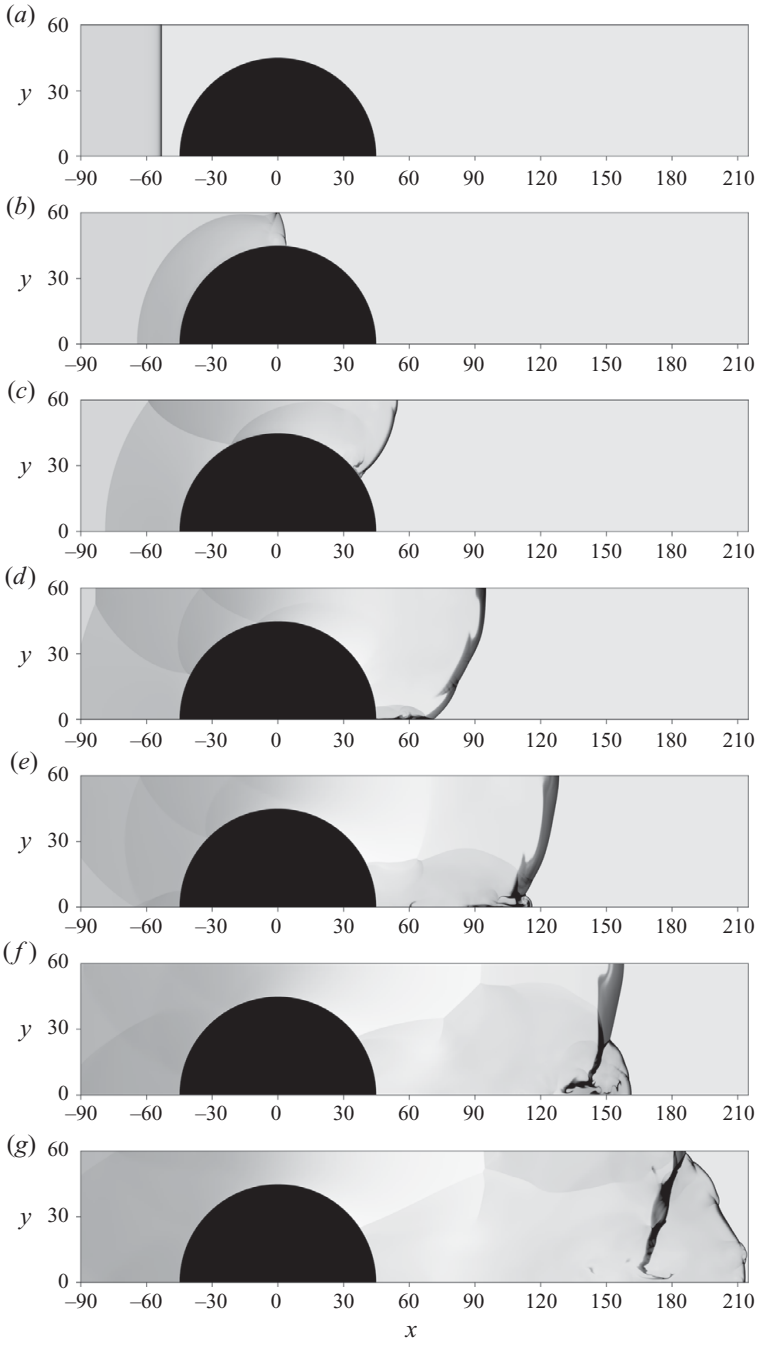

FIGURE 14. Density field evolution illustrating the detonation re-initiation from the first shock reflection for a non-dimensional pore size of $b = 30$; $(a–g)$ at $t = 0$, 5.97, 11.8, 18.7, 24.7, 30.5 and 36.3; greyscale ranging from 0 to 1 given by $(\rho - 1)/9$.

is rapidly consumed behind the Mach shock, which also develops a cellular structure characteristic of self-sustained detonations.

As can be seen from figure 15, the reactivity behind the new Mach shock is comparable with that behind a CJ detonation. Indeed, as shown in figure 16, the

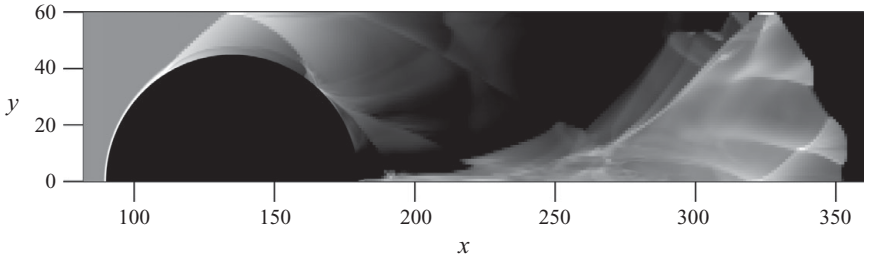

FIGURE 15. Maximum exothermicity field ξ for $b = 30$; greyscale ranging from 0 to 1 given by $(\log \xi + 0.7)/2$.

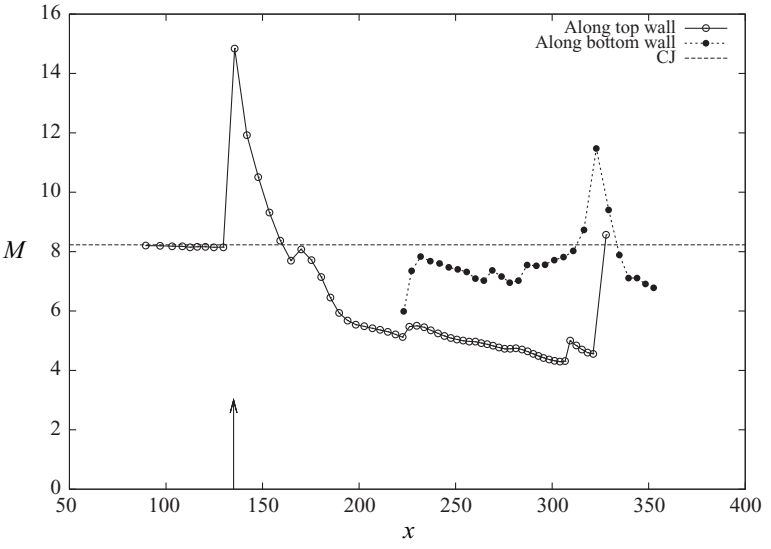

FIGURE 16. Shock Mach number recorded along the top and bottom boundaries for a pore size of $b = 30$; the arrow indicates the position of the throat.

strength of the reflected Mach shock approaches a value close to CJ. The mechanism of detonation re-initiation is thus from the reflection of the diffracted shock, which gives rise to an overdriven detonation. The wave dynamics thus follow a similar sequence as studied in the past for detonation diffraction experiments (Teodorczyk *et al.* 1988; Ohyagi *et al.* 2002; Khasainov *et al.* 2005; Sorin *et al.* 2009) and the present critical experiments illustrated in figure 3.

One notable difference between the numerical and experimental results, however, is that in the numerics, following the detonation initiation, a transverse detonation wave (super-detonation) is not observed. For example, figures 3, 6 and 7 do show such transverse super-detonations (Gamezo *et al.* 2000; Pintgen & Shepherd 2009), while in the numerical results, the transverse waves are non-reactive. This shortcoming may be due to the limitation of the one-step model, which captures correctly the appropriate induction time dependence on local state, but does not capture the narrowness of the power pulse occurring at the end of the induction process (Radulescu 2003). Future study should address this shortcoming of the one-step model. Nevertheless, the re-initiation event occurs first behind the amplified Mach shock, such that these

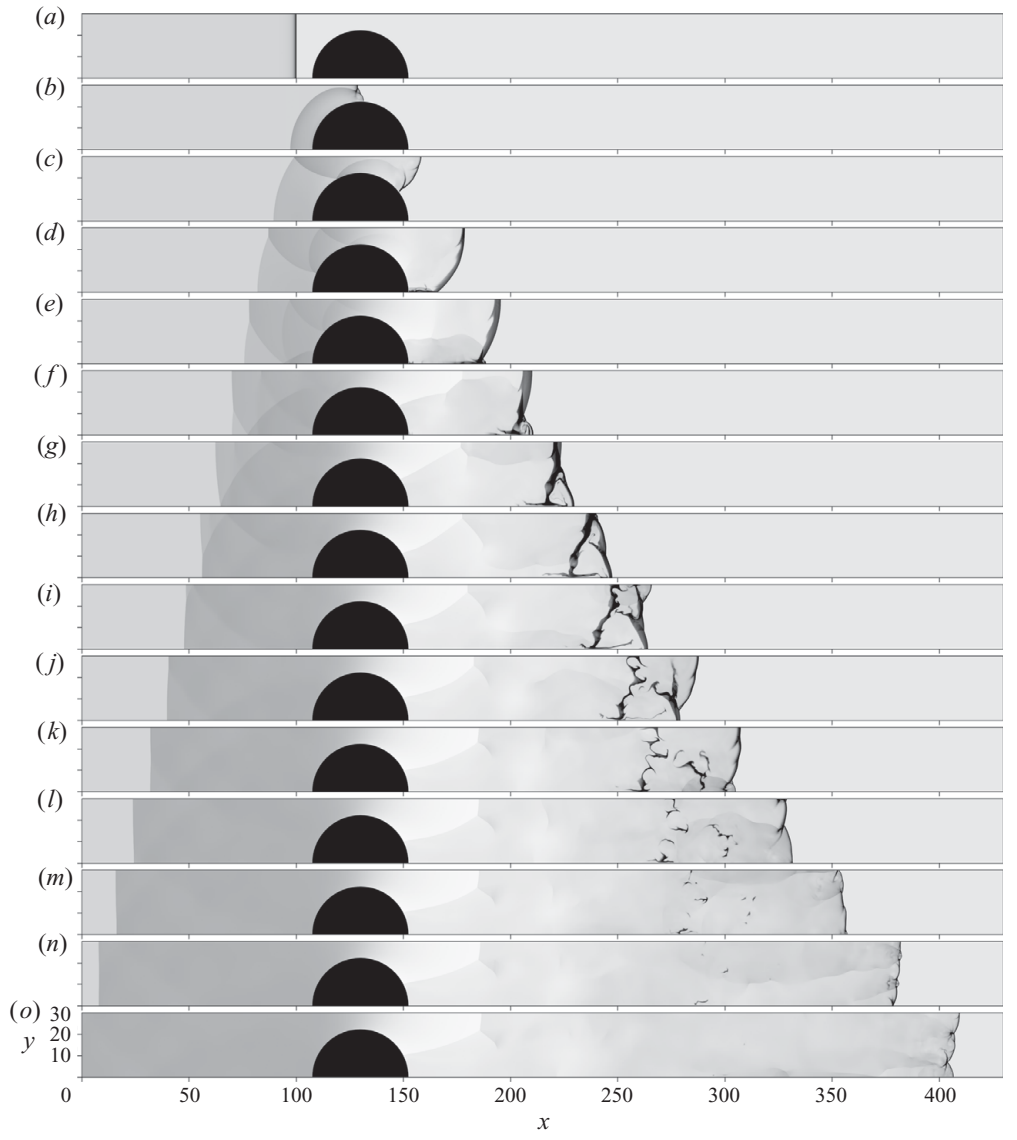

FIGURE 17. Density field evolution illustrating the detonation re-initiation from the second shock reflection for a non-dimensional pore size of $b = 15$; $(a–o)$ at $t = 0$, 3.24, 6.07, 9.47, 12.5, 15.5, 18.4, 21.3, 24.2, 27.0, 29.8, 32.6, 35.4, 38.1 and 40.9; greyscale ranging from 0 to 1 given by $(\rho - 1)/9$.

super-detonations are a consequence of the detonation re-establishment. In the experiments, no super-detonations are observed prior to the detonation formation.

4.1.3. $b = 15$

As the pore dimension is further reduced from $b = 30$ to $b = 15$, the initial diffraction around one cylinder continues to quench the detonation. However, the subsequent wave reflections with the walls of the channel give rise to a flow field of increasing complexity. Figure 17 shows the evolution of the density field for $b = 15$, while figure 18 shows the maximum rate of energy release obtained during the entire

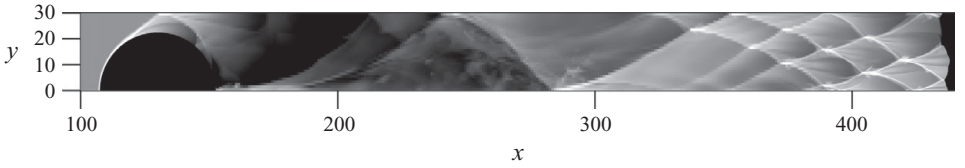

FIGURE 18. Maximum exothermicity field ξ for $b = 15$; greyscale ranging from 0 to 1 given by $(\log \xi + 0.7)/2$.

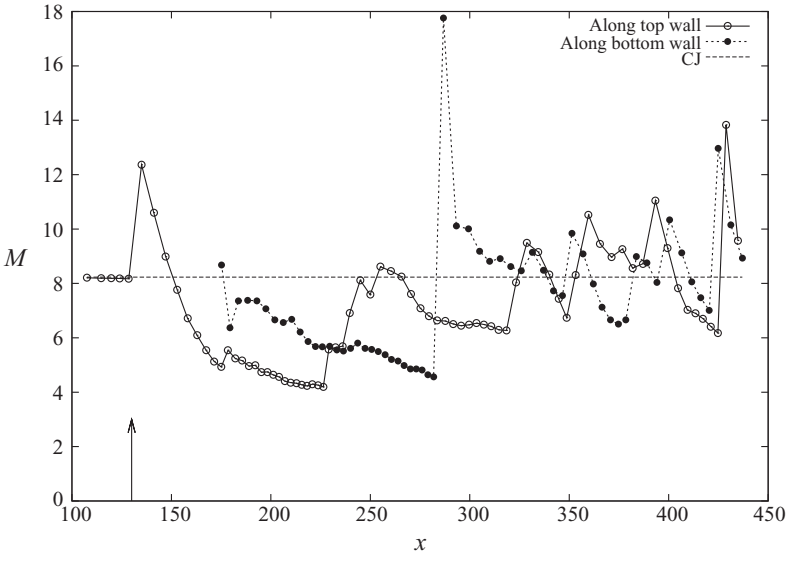

FIGURE 19. Shock Mach number recorded along the top and bottom boundaries for a pore size of $b = 15$; the arrow indicates the location of the throat.

calculation in the domain, analogous to the open-shutter photographs. The Mach number measured along the top and bottom walls is shown in figure 19. A detail of the diffraction process is given in figure 20, while figure 21 shows the density, pressure, temperature, gas velocity, absolute reaction progress variable and reaction rate given by

$$\rho \frac{\mathrm{D}\alpha}{\mathrm{D}t} = \rho k(1-\alpha)\mathrm{e}^{-E_a/RT}, \tag{4.2}$$

at one particular time during the transient leading to the detonation re-establishment.

The initial reflection of the detonation wave on the cylinder, illustrated in figure 17, gives rise to an overdriven detonation wave. Its diffraction around the cylinder leads to a significant slow down of the reactions, similar to the results described above for $b = 30$. What is interesting, however, is the reflection of the diffracted detonation wave on the bottom boundary occurring in figure 17(*d*,*e*). As can be seen from figure 18, this reflection of the diffracted shock gives rise to faster reaction rates behind the resulting Mach stem. Indeed, a new Mach stem of strength less than CJ (see figure 19) is driven into the unreacted gas. As can be seen in figure 17(*e*–*g*), shown in more detail in figure 20, the gas behind this Mach stem initially reacts rapidly. However, this shock reflection does not give rise to a self-sustained detonation, and the Mach stem continues to decay. As the strength of the wave drops, the rate of energy release

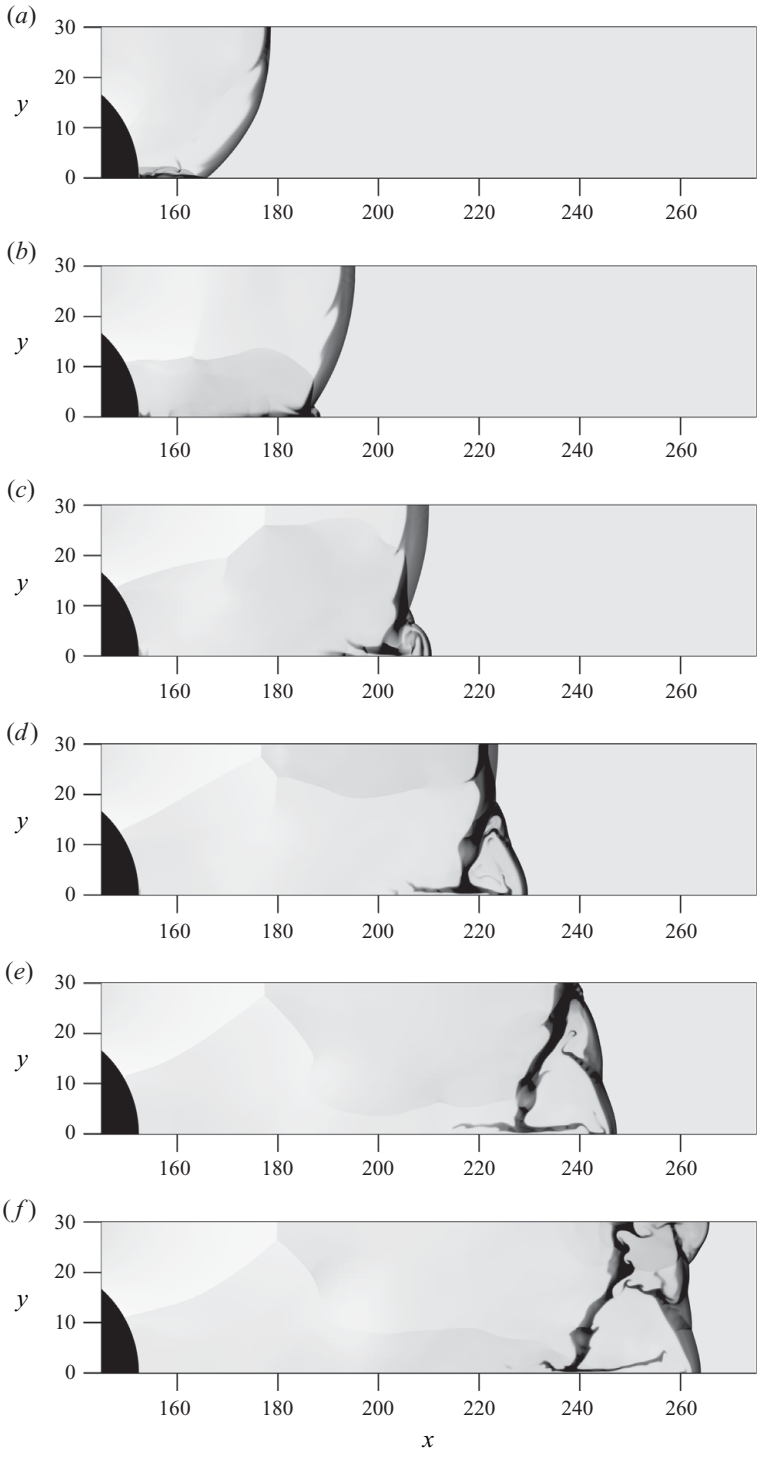

FIGURE 20. Detail of figure 17; (*a–f*) at $t = 9.47$, 12.5, 15.5, 18.4, 21.3 and 24.2.

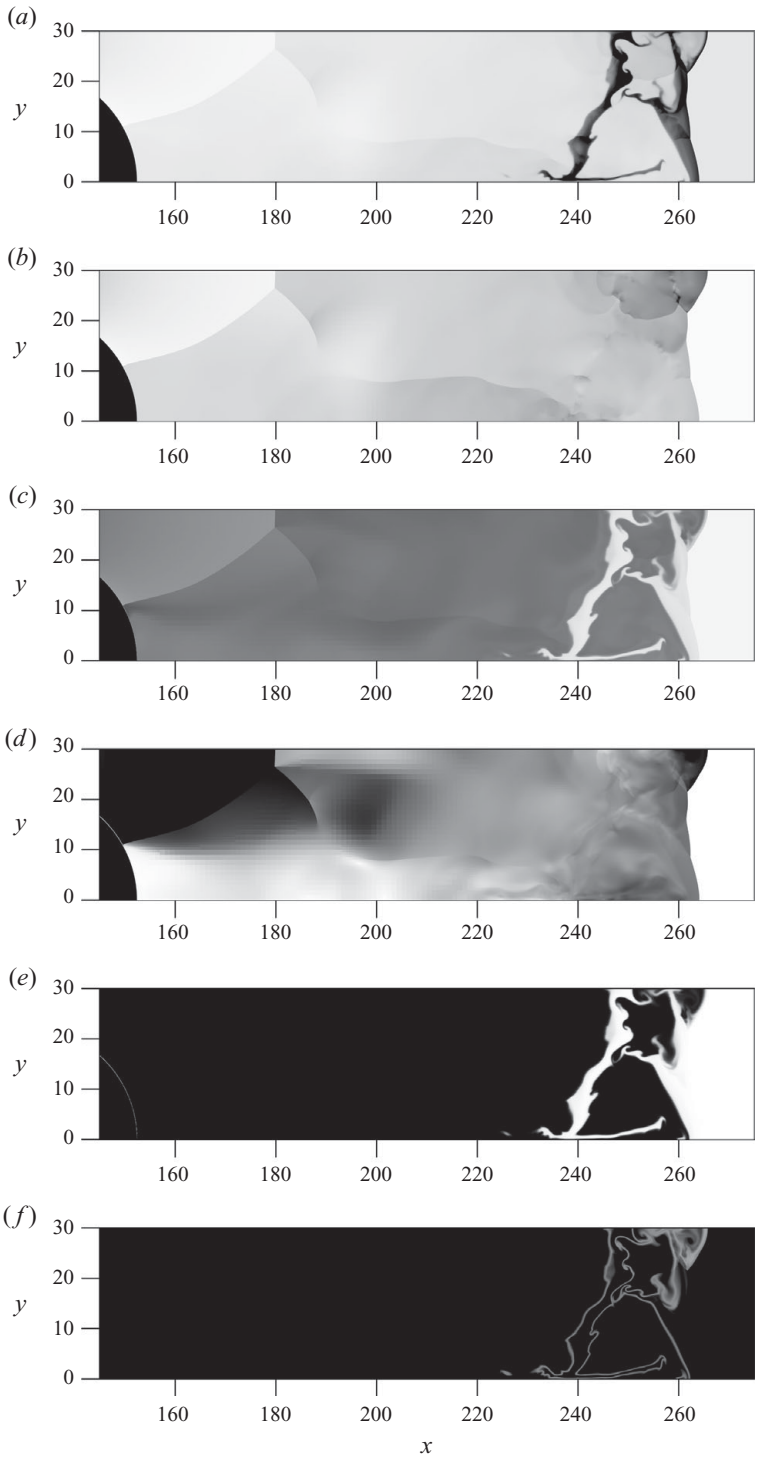

FIGURE 21. Greyscales illustrating (*a*) the density field $((\rho - 1)/(10 - 1))$, (*b*) pressure field $((p-1)/(100-1))$, (*c*) temperature field $((T-1)/(30-1))$, (*d*) absolute gas velocity $(\sqrt{u^2 + v^2}/8)$, (*e*) reaction progress variable α and (*f*) reaction rate $(\log(p\mathrm{D}\alpha/\mathrm{D}t) + 1)/3$ at $t = 24.2$.

behind the shock is also reduced, as can be seen from figure 18. As a result, the reaction zone becomes much thicker, as can be seen from figure 20.

The reflection of the subcritical Mach stem on the top boundary (between figures 17*h* and 17*i*) also gives rise to a new Mach stem, which undergoes the same subcritical decay as the previous one, as can be seen in figure 17(*i–k*). Note that both subcritical reflections give rise to two large layers of burned gases alternating with layers of unburned gas, which fall behind the leading front as more gas is engulfed by the front. The long lifetime of these unreacted pockets, which can be traced in figure 17(*l–o*), illustrate well that the reactions rates are very low, with the exception of the periodic 'hotspots' created when the waves reflect.

The instantaneous flow field is shown in figure 21 in terms of the density, pressure, temperature, velocity, reaction progress variable and reaction rate. On comparison of the density, temperature and reaction progress variable, the flow fields illustrate that the pockets of high density gas accumulating behind the front are pockets of non-reacted gas at low temperature. The reaction rate field is most instructive, in that it shows that the interior of these pockets undergoes a very slow reaction process (below less than two orders of magnitude of the CJ value), while only the gas behind the Mach stem has a high reaction rate. Note that the boundaries of the pockets react nevertheless by numerical diffusion due to the capturing of these contact surfaces on a finite grid (Radulescu *et al.* 2007). The physical picture that emerges is that wave reflections give rise to local hotspots, while the bulk of the gases remain un-reacted on long time scales.

It is only after figure 17(*k*) that a self-sustained detonation is re-initiated. Re-initiation here is associated with the third main shock reflection with the bottom wall, which yields a self-sustained detonation, with its characteristic cellular structure.

The physics of the global re-initiation process through the two failed re-initiation events can be best understood by investigating figures 18 and 19. Each subcritical reflection, although individually not sufficient to re-establish the detonation wave, gives rise to an acceleration of the reaction rate and consumption of large layers of reactant. After each reflection, the lead shocks experience a global acceleration from the large portions of gas having reacted. It thus appears that although the local mechanism of acceleration of reaction rates is associated with wave reflections, the global acceleration involves the integrated effect of exothermicity on the leading front, which undergoes a global acceleration process. The shock reflections can thus be viewed as a sequence of steps that the high-speed deflagration takes to accelerate back to a self-sustained detonation.

4.2. *Attenuation and re-initiation from multiple cylinders*

Further numerical experiments were performed to investigate the role played by multiple columns of cylinders in the detonation's path. We focused on one single mixture sensitivity corresponding to a pore size of $b = 15$, and considered the detonation interaction with one, two or three successive cylinders and its subsequent re-amplification. Figure 22 illustrates the density field evolution in the case of three cylinders. The evolution shown in figure 22(*a–d*) is identical to that illustrated in figure 17. In figure 22(*e*), the decaying diffracting wave is reflected on the second cylinder, while in figure 22(*f*), the wave reflects on the bottom boundary. These recompressions generate local regions of high temperature which accelerate the reaction rates, as can be seen in figure 23.

The presence of a third cylinder gives rise to the same history of wave reflections, as can be seen in sequence of interactions between figures 22(*h*) and 22(*n*). It is interesting

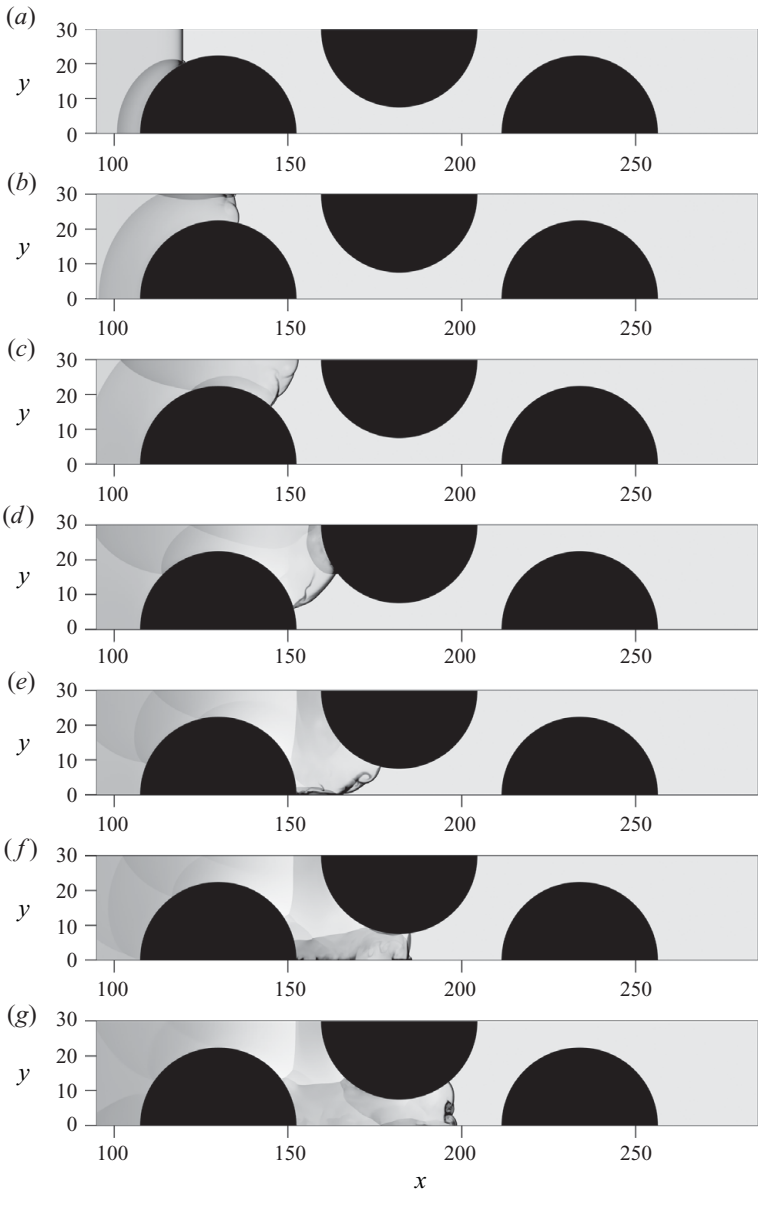

FIGURE 22. (*a–g*) For caption see facing page.

to note that the emergent wave from three cylinder interactions is a relatively thin reaction zone front, similar to the emergent wave from the interaction with a single cylinder. This result suggests that a local detonation is maintained after each cylinder interaction, as also suggested by the experimental observations in § 2.

The weak dependence of the number of cylinders on the detonation is further confirmed in figure 24, where the strength of the emergent wave is compared after one, two or three cylinder interactions. As can be seen, the strength of the detonation wave at a distance of 50 half-reaction lengths downstream of the last throat, which

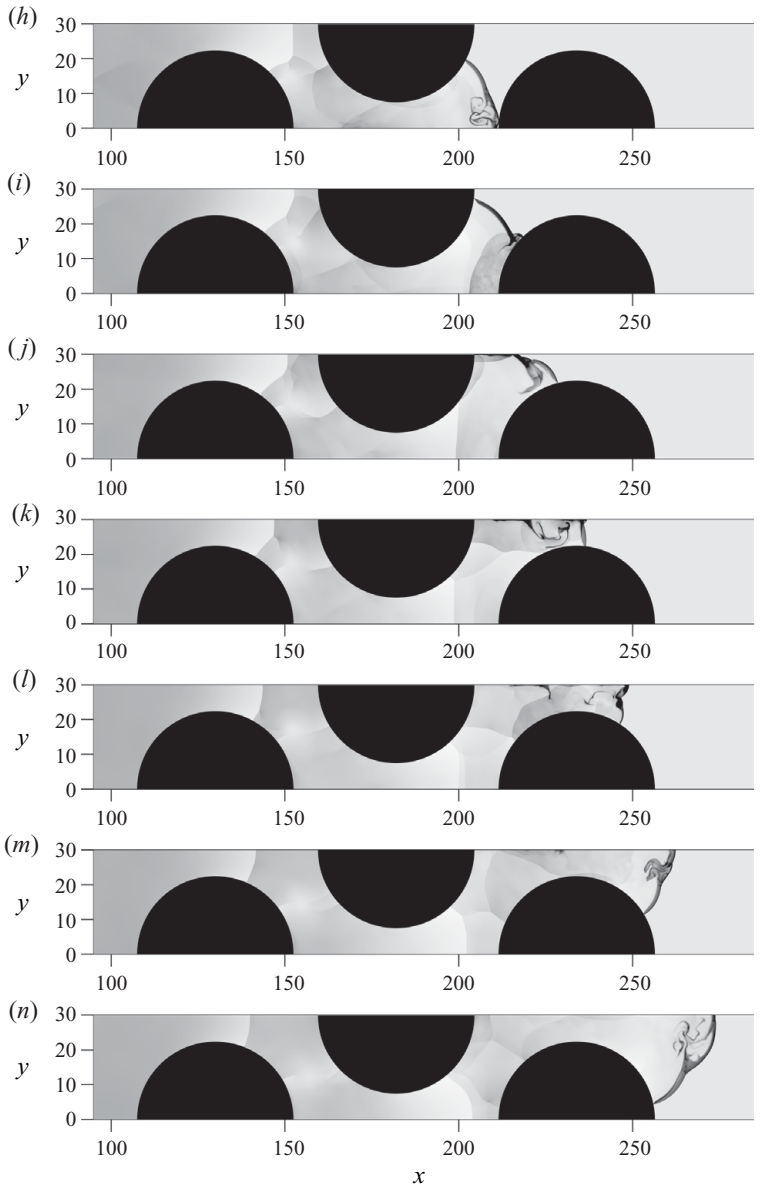

FIGURE 22. Density field evolution illustrating the detonation passing through three columns of cylinders for a pore size of $b = 15$ at $t = 2.23$, 3.74, 5.41, 7.46, 9.47, 11.3, 13.1, 14.9, 16.7, 18.4, 20.3, 22.1, 23.9 and 25.8; greyscale ranging from 0 to 1 given by $(\rho - 1)/9$.

represents approximately one cylinder diameter, is very similar for the three different cases.

In spite of the similarities in wave strengths, the re-initiation of the detonation in the critical regime appears to be affected somewhat by the number of cylinders, as can be seen from the long time evolution illustrated in figure 24. The re-initiation occurs systematically at a greater distance from the last cylinder as the number of cylinders is increased. This may be due to the extreme sensitivity of the reaction rates on temperature, which plays a crucial role in the amplification process. For example,

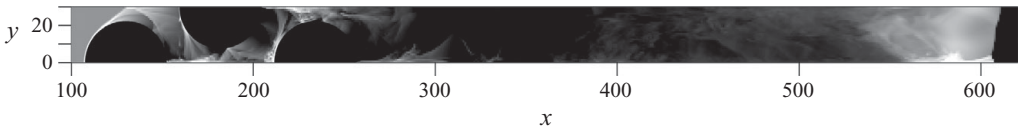

FIGURE 23. Maximum exothermicity field ξ for $b = 15$ for the detonation attenuation by three cylinders; greyscale ranging from 0 to 1 given by $(\log \xi + 0.7)/2$.

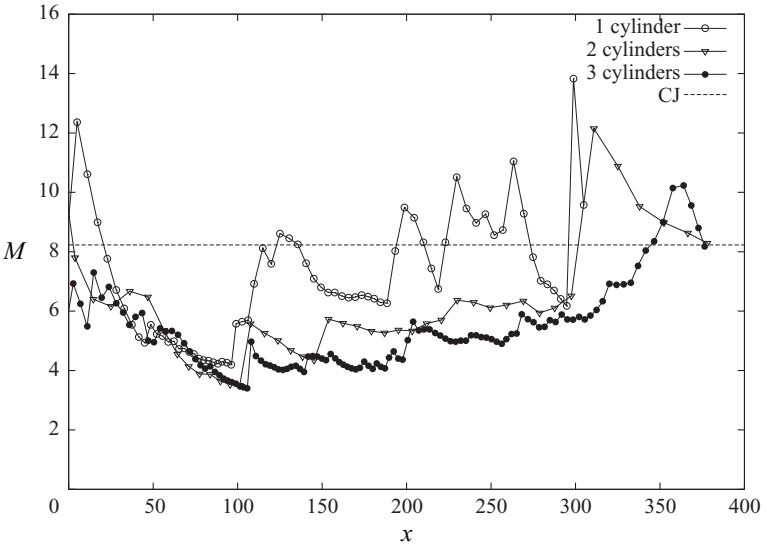

FIGURE 24. Shock Mach number recorded along the axis of the last throat after a detonation interaction with one, two and three cylinders for a pore size of $b = 15$; the origin of the x-axis is the location of the last throat in all cases.

figure 22 shows that after three interactions with the cylinders, a small amount of gas remains unreacted. This in turn will modify the strength of the transmitted wave and trailing flow field, and hence modify the entire re-acceleration sequence, which depend not only on the shock strength, but also on the gas dynamic field behind it.

The mechanism of acceleration, however, is the same for one, two or three cylinders. Figure 25 shows the gas dynamic details of the acceleration process after the interaction with three cylinders. Figure 25(a–f) shows the first subcritical reflection of the diffracted wave on the bottom boundary. Following the first reflection, a large portion of gas ignites behind the Mach shock, and through its expansion, provides a gas dynamic driving mechanism to the front, which bulges out near the bottom of the photograph. The Mach number record of figure 24 shows clearly this acceleration event.

The subsequent reflection on the top wall, which occurs between figures 25(d) and 25(e), also gives rise to an increase in exothermicity. A pocket of gas near the top wall does not ignite until it reaches the state shown in figure 25(i,j). The gas dynamic history of this gas was difficult to retrace due to the numerous wave reflections. Similarly, numerous ignition spots can be seen within the layer of unreacted material. The detonation formation between figures 25(i) and 25 (j) appears to culminate from the sequence of wave reflections and global acceleration, as illustrated in figure 24. The likely mechanism for global wave acceleration and transition to detonation appears to correlate with the reactivity of the gas within the reaction zone structure, favoured by 'hotspot' formation of increased reactivity. The almost smooth

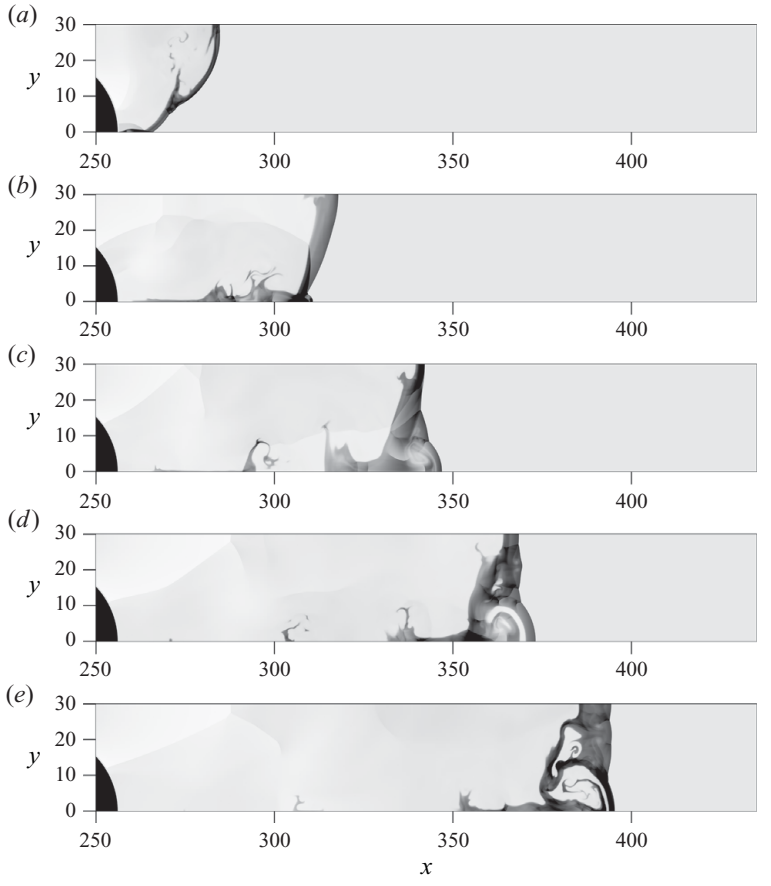

FIGURE 25. (*a–e*) For caption see next page.

acceleration process illustrated in figure 24 suggests that a global hydrodynamic statistical model for the acceleration process is worthwhile.

4.3. *Grid resolution effect*

The effect of grid resolution was investigated for the pore size of $b = 15$, where the long re-initiation transients would most likely be affected by grid resolution effects. The results presented in figure 17 for a pore size of $b = 15$ were also computed with a higher (64 grid points per half-reaction length) and lower resolution (16 grid points per half-reaction length). Very good agreement was found between the results obtained with different resolutions for the entire acceleration process. Figure 26 shows the density profiles obtained just before the onset of detonation. As can be seen, the various features of the wave dynamics have been well reproduced with different resolutions. The various wave reflections on the wavefront are at the same location. More importantly, however, is that the unreacted gas behind the front is not affected significantly by the resolution, although, as demonstrated in figure 21, the boundaries of the unreacted pockets are consumed by numerical diffusion. A more rapid burnout of the unreacted layers of gas is, however, observed at the lower resolutions, consistent with the fact that the numerical diffusion rate is effectively larger at lower resolutions (Radulescu *et al.* 2007). Similarly, instabilities on the surface of the layers of unreacted

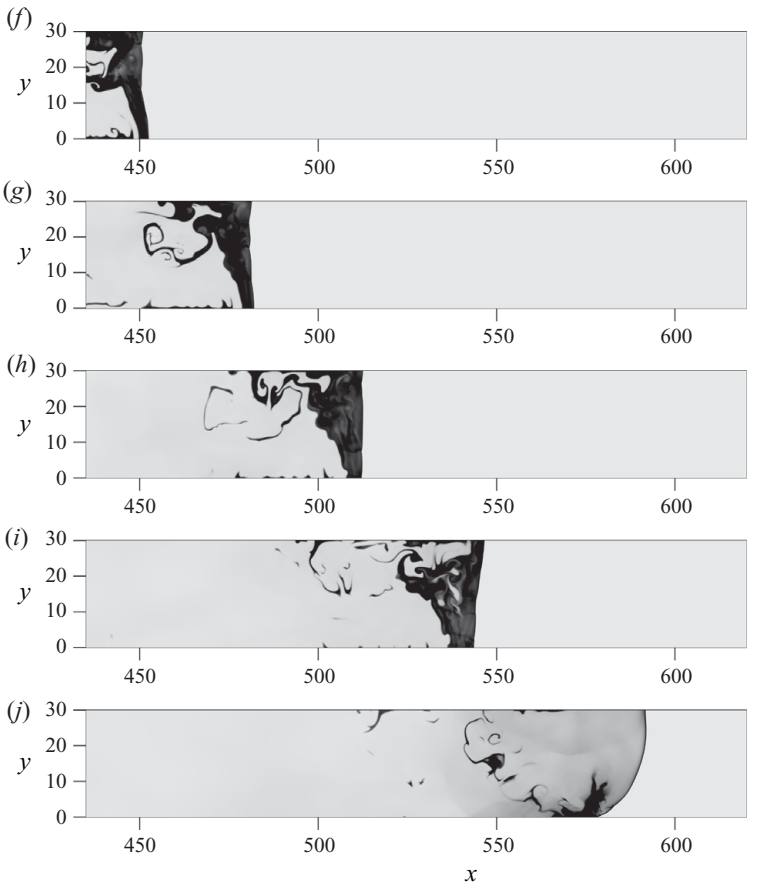

FIGURE 25. Density field evolution after the interaction of a detonation wave with three columns of cylinders for a pore size of $b = 15$; $t = 27.7$, 34.1, 40.2, 46.0, 51.5, 57.0, 63.1, 68.7, 74.2, 79.7 and 85.3; greyscale ranging from 0 to 1 given by $(\rho - 1)/9$.

gas are better resolved at higher resolution. These are very similar to what is observed in the reaction zone structure of highly unstable detonations (Radulescu *et al.* 2007).

The more rapid burnout of the unreacted pockets at lower resolution has the effect of somewhat enhancing the reaction rates behind the accelerating front and promoting the acceleration process. This very weak effect can be seen in figure 27, where the history of the maximum exothermicity is shown for the three different resolutions. As can be seen, there is a slight propensity for a more rapid acceleration and higher levels of exothermicity closer to the cylinder at the lower resolution.

5. Discussion

5.1. *Limits*

In the experiments, the critical conditions for direct propagation of a detonation through the porous section were such that the pore size was approximately equal to two to three cell sizes λ. Our calculations show that for the present mixture, the cell size is related to the chemical induction layer, which is assumed to serve as a good approximation to the half-reaction length, $\Delta_{1/2}$, by $\lambda \approx 36\Delta_{1/2}$ (see table 1). Thus we would expect criticality at approximately a pore size equal to 70–110 half-reaction

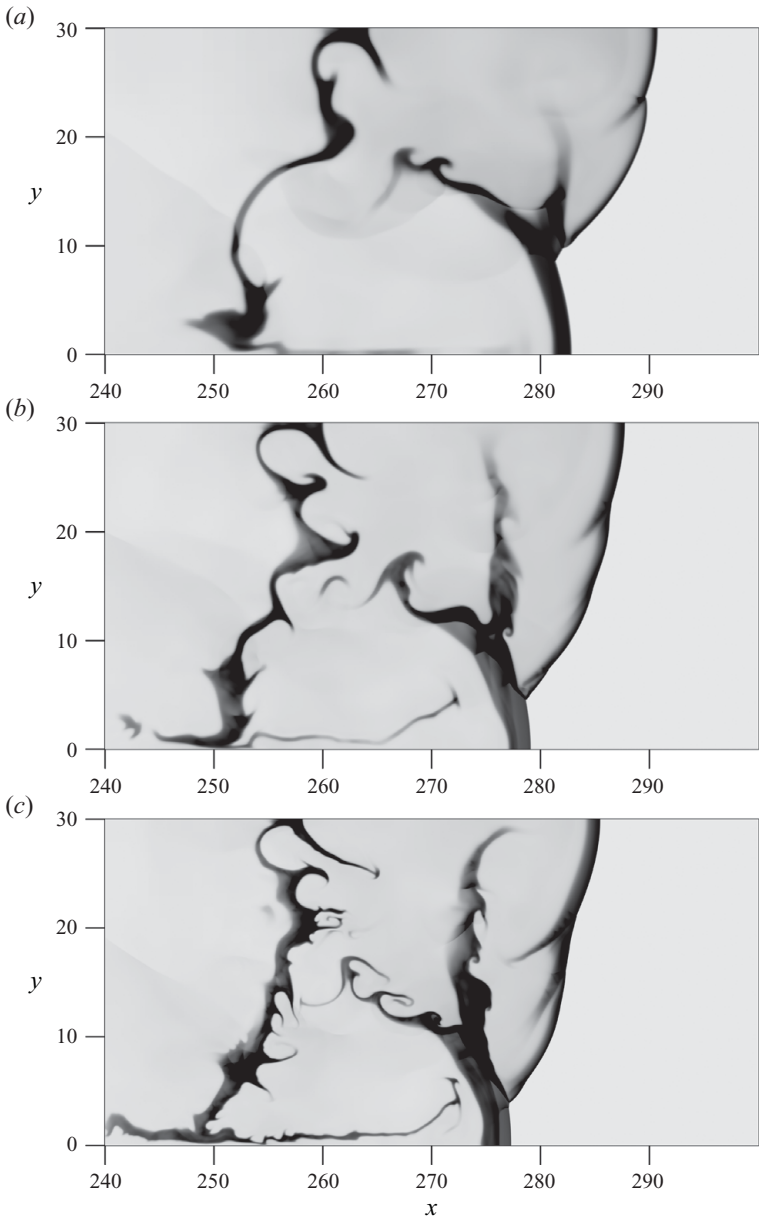

FIGURE 26. The flow field established prior to the onset of detonation for $b = 15$ for different grid resolutions of 16 points/$\Delta_{1/2}$ (*a*), 32 (*b*) and 64 (*c*).

lengths. This is in reasonably good agreement with the current calculations, which show that criticality is expected at a pore size bracketed between 30 and 60 half-reaction lengths. The results differ by a factor of 2. This agreement is quite remarkable, in view of the number of simplifying assumptions adopted in the present model (one-step chemistry, two-dimensional flow field, inviscid simulations). Unfortunately, we cannot gain further insight from this difference because the thermo-chemical database used to determine the reaction zone thickness is itself not more accurate than a factor of 2. Indeed, comparison of the kinetic model predictions of ignition delay with the

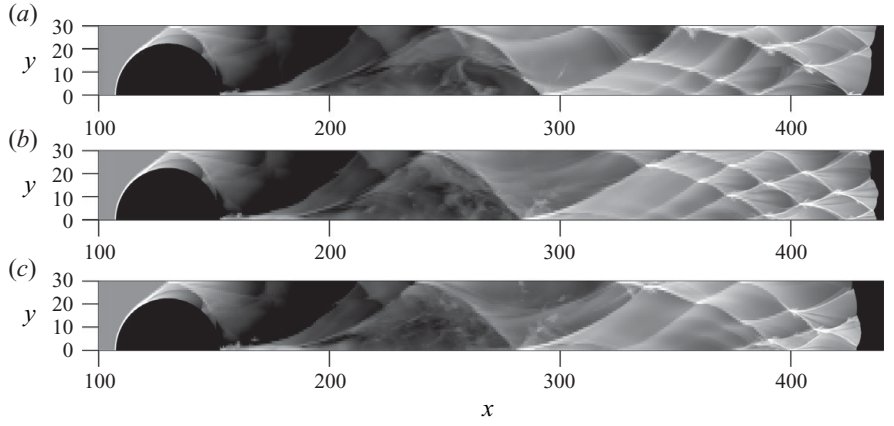

FIGURE 27. The maximum exothermicity field for the detonation formation after the interaction with one cylinder and pore size $b = 15$ for different grid resolutions of 16 points/$\Delta_{1/2}$ (a), 32 (b) and 64 (c).

available experimental ignition delay data obtained using reflected shocks yielded agreement within a factor of 5 (Varatharajan & Williams 2001). The only logical conclusion is that we have very good agreement, within the confidence of the existing available kinetic models.

The limit for re-initiation behind the cylinders involving more than two reflections ($b = 15$ in numerics) appears to be somewhat different than in the experiments, which occurs at approximately 5 kPa initial pressure, corresponding to a value of pore size equal to approximately 60 induction lengths or approximately two cell sizes. The experimental and numerical limits are thus different by a factor of 4. It thus appears that the scaling of the mixture sensitivity with size of the domain between the critical transmission and initiation via two reflections is different in the experiment and in the numerics. In the experiments, the range over which one passes from direct transmission to non-transmission is much narrower than in the numerical simulations, by roughly a factor of 2. Our speculative explanation, consistent with the behaviour of detonations at reduced pressure in our apparatus, is the role played by heat and boundary layer losses in the narrow channel. These effects were not incorporated in the numerical treatment. The experiments showed that when the cell size of the mixture was larger than approximately twice the channel thickness, losses affected the detonation propagation upstream of the porous section, and the detonation and combustion could even be altogether extinguished either in the porous section or at its exit. This extinction can only be accounted for by boundary losses, otherwise, a flame would always be observed following the detonation decoupling into a shock-deflagration complex. Due to these non-idealities, further comparison between experimental limits and numerically determined limits was not attempted.

5.2. *Limitations of the one-step model*

The numerical part of the present paper investigated the dynamics of detonation attenuation and re-initiation by using the simplest one-step Arrhenius reaction model. Although very important in its own right, the simplified model does not reproduce some experimentally observed features. One of the failures of the one-step model is its inability to capture the chain-branching character of the reactions and the corresponding cross-over effect (Varatharajan & Williams 2001). This character

provides a change in the shock sensitivity of the reaction rates if the shock strength falls below a critical value. The cross-over behaviour can essentially make the distinction between successful transmission and failure much more sharp by suddenly modifying the ignition delays beyond the cross-over threshold. This could explain some of the observations made in the previous section.

Another failing of the one-step model dynamics is its inability to capture the super-detonations observed in the experiments upon the detonation re-initiation. At present, the reason for this failing is believed to stem from the much longer power pulses predicted by the one-step model in the reaction zone; the maximum thermicity (i.e. the rate of energy release) in the reaction zone is much larger when predicted with the real kinetic mechanisms than in a one-step model with the same induction zone sensitivity. The consequence of this shortcoming of the one-step model on the re-acceleration mechanism before the onset of detonation is unclear. Future study should clarify the importance of the magnitude of the power pulse on the coupling between gas dynamics, reactivity and energy release.

5.3. *Comparison with previous experiments in porous media*

Makris (1993) has performed an extended study of detonation propagation in a porous medium and measured the velocity deficit. Using his experiments and previous experiments performed in obstacle-laden tubes and other porous media, he suggested a scaling such that all results collapsed onto a single approximate velocity-deficit-dependence curve. For each detonatable mixture, the geometrical scaling corresponded to the ratio of the cell size, denoting the sensitivity of the mixture, to the pore size, which he defined as the square (or cubic, in three dimensions) root of the open area of the successive pores. He found that the transition between fast propagating quasi-detonations and low-speed deflagrations propagating at velocities less than approximately 50 % of the CJ velocity corresponded to approximately a pore size characteristic dimension equal to one to two cell sizes. This value is found to be in good agreement with the current findings. It corresponds to the conditions when the detonations are quenched following the diffraction around the obstacle and do not re-ignite until more than two reflections with the bounding walls. Thus it appears that this critical transition marks the boundary at which shock reflections may permit rapid ignition.

5.4. *The re-initiation transient*

The numerical simulations of the transient re-initiation period have revealed that the re-establishment of a detonation following the attenuation by the porous medium relies on one or multiple wave reflections with the bounding walls, depending on the mixture sensitivity. The length scale for this re-establishment transient was found to be approximately 200–300 ZND half-reaction lengths. During this transient, the front decays to approximately half the CJ velocity. During this transient, the re-initiation mechanism consisted of multiple shock reflections, which individually can ignite large amounts of unreacted gas. Each reflection did not necessarily lead to the onset of detonation. Instead, each reflection participates in slowly re-accelerating the front.

The applicability of the new re-ignition mechanism to real systems remains uncertain because of the deficiency of the numerical model in reproducing super-detonations. However, the new re-initiation mechanism deduced from the above numerics is consistent with the photographs reported by Makris *et al.* (1993) in the critical regime of initiation. Figure 28 shows a sequence of schlieren photographs taken by Makris illustrating the evolution of an acetylene–oxygen–argon detonation wave interacting with one column of half-cylinders. Although the images do not clearly resolve the gas

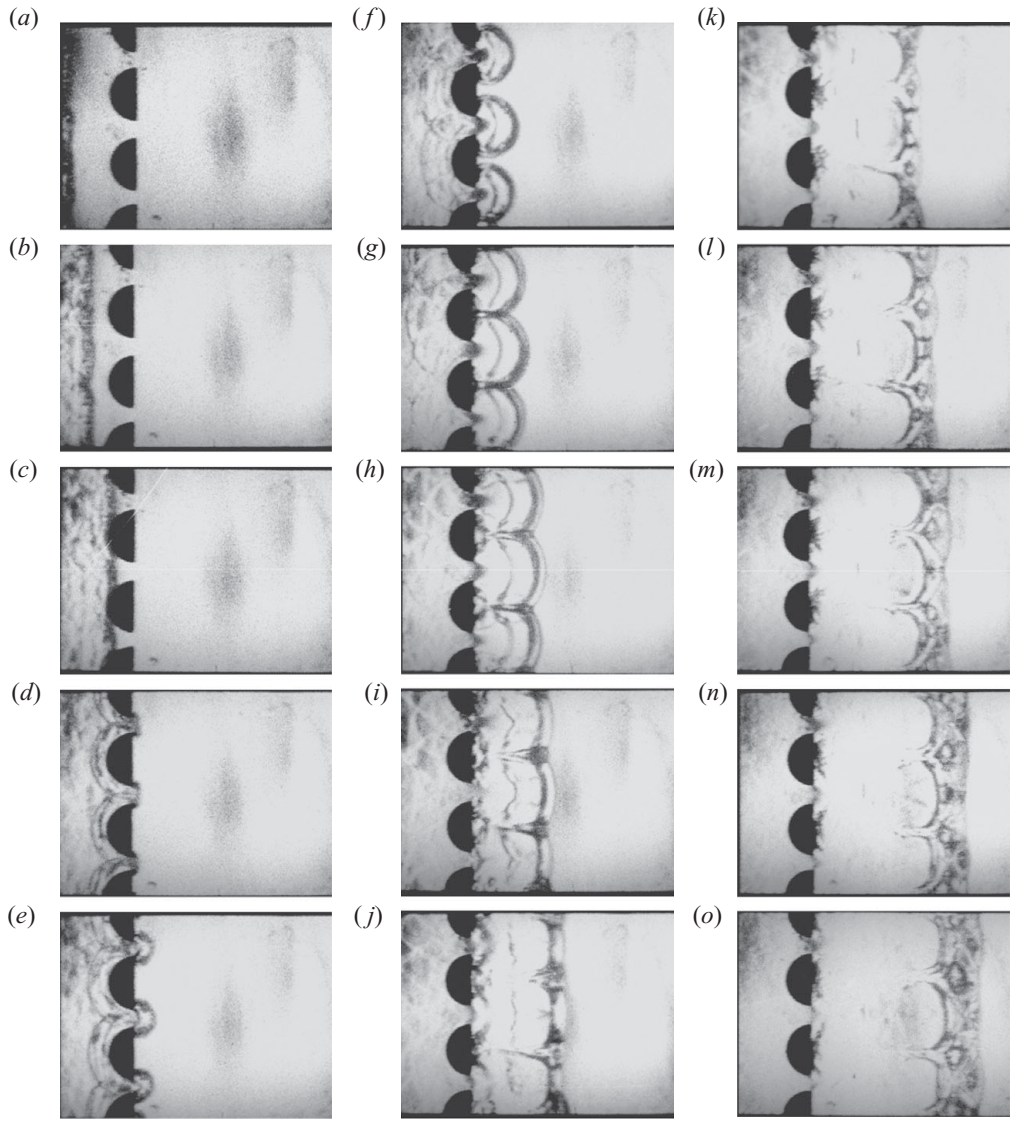

FIGURE 28. Sequence of schlieren photographs illustrating the detonation quenching and discrete ignition centres after a detonation interaction with half-cylinders for $b/\lambda \approx 0.5$; mixture is $C_2H_2 + 2.5O_2 + 75\,\%$Ar at 7.5 kPa, the distance between cylinders is 8.5 mm and the inter-frame time is 7.12 μs. (Photographs courtesy of A. Papyrin.)

dynamic details, the onset of discrete reaction spots can be clearly observed through the same sequence as in the numerical experiments above. Figure 28(*e*,*f*) shows the diffracting shocks originating from the individual pores. In figure 28(*h*), the shock and reaction zone have separated. The interaction between the diffracting heads, occurring at figure 28(*f*), gives rise to a series of new Mach shocks and ignition sites clearly visible in figure 28(*k*). Similarly, the second generation of ignition spots can be seen in figure 28(*n*,*o*); these originate from the second generation of shock reflections, as illustrated in figure 17. The resulting reaction zone structure thus consists of a layered structure of the reacted and unreacted gas, very similar to the numerical flow fields established above.

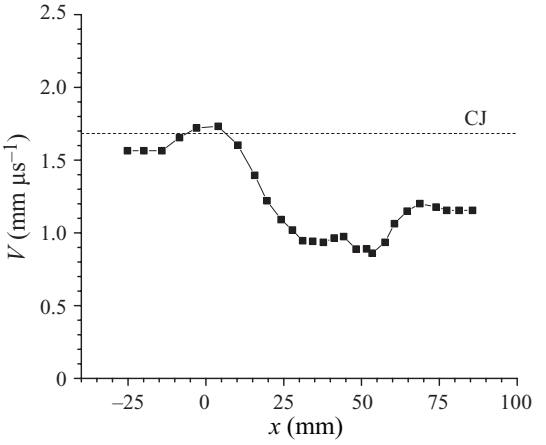

FIGURE 29. Mean wavefront speed along the three pore axes deduced from the experiment shown in figure 28.

We have re-examined the entire set of experimental frames leading to figure 28, which shows only every second available frame. From the digitized photographs, we determined the position of the leading front along the axis of each pore. Averaging the three sets of data for each pore, we obtained the average position of the front. Then the velocity was obtained by a second-order estimation among neighbouring points. The resulting velocity evolution is shown in figure 29. Very similar to the numerical records, the velocity increases when the front passes through the throat, and then rapidly decays to approximately half the CJ velocity. As can be seen, there are two sequential amplifications of the front, which correlate with the location of hotspot ignition in the first-generation shock reflection and second-generation shock reflections.

The re-initiation mechanism identified in the present study may also shed some light on previously observed wave propagation and acceleration regimes. For example, Chao (2006) and Zhu *et al.* (2007) studied the re-establishment of the detonation wave following the interaction with a perforated plate. In that study, the authors assume that following the interaction with the plate, the detonation wave is quenched. The reaction products jetting out through the holes of the perforated plate then mix with the non-reacted gases shocked by the transmitted shock, establishing a metastable wave which then transits to a detonation. In the present study, we see that the detonation wave is indeed quenched upon its diffraction from each pore due to the expansion cooling. However, the shock ignition mechanism is maintained in discrete regions where shock reflections occur, extending on length scales of 300 detonation half-reaction lengths downstream of the exit section. These shock reflections were found to be able to sustain a slowly accelerating 'metastable' wave. In our numerical experiments, turbulent mixing does not play any role. Turbulent mixing, however, cannot be ruled out.

5.5. *Diffusive transport: dog or tail?*

In our numerical experiments, during the re-initiation transient, which lasts approximately 300 half-reaction lengths, turbulent mixing does not play any role. The minimal numerical diffusion only slightly affects the amplification process, as discussed above. In the experiments, however, there are indications that turbulent mixing is active. Very bright bands were observed in the open-shutter photographs (figure 7) prior to the detonation formation, and these could not be reproduced with

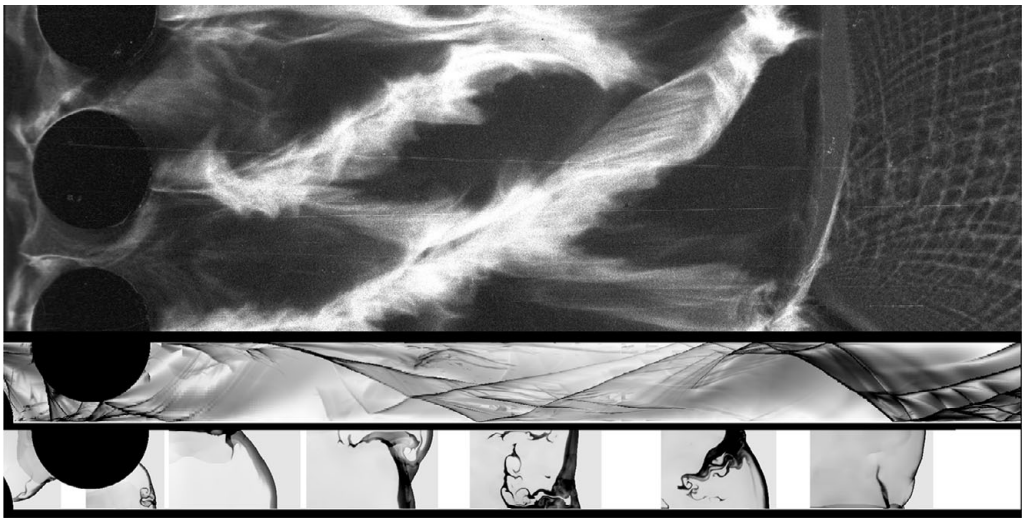

FIGURE 30. Comparison between the open-shutter photograph of figure 7 (top) and the flow field established after the detonation interaction with two cylinders for $b = 15$; the integrated maximum vorticity (middle) and the sequence of seven density profiles (bottom) obtained numerically illustrate that the luminous streaks of the experiments match the trajectories of the triple point interactions, where high vorticity is recorded.

the Euler simulations of the numerical treatment. Such bright luminosity events have also been observed by Austin (2003), Radulescu *et al.* (2005) and Kiyanda (2005) on the boundaries of unreacted pockets in unstable detonations. The question that arises is whether diffusive transport plays an important role in the experiments in dictating the re-initiation transient (the dog), or whether it is only a weak consequence of the unsteady gas dynamics (the tail), inconsequential to the acceleration process. This section attempts a tentative answer based on analysis of the flow field and deflagration velocity in the shocked unreacted gases driven by diffusive processes.

To study the origin of the bright bands observed in the experiments, we have first compared the numerical simulations with the experimental records. Figure 30 shows a part of figure 7 obtained for $b = 15$ and two cylinders alongside the two numerical records. The first record, immediately below the experiment, shows the integrated maximum vorticity field. Below it are shown seven density profiles of the same numerical experiment, which helps in the interpretation of the vorticity record. The vorticity record permits us to determine the path of triple points at the front, where the vorticity is at its maximum. As can be seen, the paths of the bright bands observed in the experiments agree well with the trajectory of the triple points in the shock-deflagration complex. It is thus reasonable to attribute the intense luminosity to the turbulent mixing that would occur at the shear layers accompanying the triple shock motion, where burned and un-burned gases are in contact, analogous to the numerical diffusive burning of figure 21 and the observations of Kiyanda (2005) and Austin (2003) and further analysis in Radulescu *et al.* (2007) and Massa, Austin & Jackson (2007) for turbulent diffusive burning in detonations.

In order to better assess the potential effect of diffusive burning in the high-speed deflagration zone, we have computed the hypothetical laminar flame speed in acetylene–oxygen mixtures at the thermodynamic conditions prevalent behind the shock wave in the high-speed deflagration wave. The state behind a shock propagating into the test gas (5 kPa and 300 K), with a Mach number of 4.1 (corresponding to approximately half the CJ velocity) was computed with realistic thermodynamic data

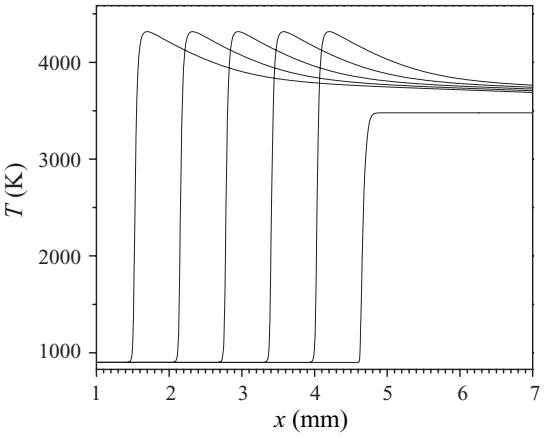

FIGURE 31. Temperature profiles illustrating the propagation of a one-dimensional planar laminar flame from a hotspot in a mixture of $C_2H_2 + O_2$ at 900 K and 1 bar; successive profiles taken at 21 μs intervals.

using the CEA code, yielding a temperature of 900 K and a pressure of approximately 1 bar. The laminar flame speed at these conditions was determined in separate calculations using a Lagrangian code developed by Maxwell (2010), which integrates the unsteady motion of the flame in the low-Mach-number approximation prior to the 'bulk' ignition of the gases. The simulations were initialized by initially imposing a jump in species and temperature profile, to simulate the burned–unburned interfaces in the deflagration structure. Using the full Sandiego mechanism (Varatharajan & Williams 2001) and assuming mixture-averaged transport properties, the laminar burning velocity was found to be 30 $\mathrm{m\,s^{-1}}$. Figure 31 shows the evolution of the temperature profile illustrating the laminar flame propagation following the hotspot ignition. Note that in this case, the adiabatic ignition delay in the un-reacted gas is $\sim 10^{-2}$ s and the laminar flame is not affected by reactions ahead of it for the short time scales considered here. The gas velocity behind the half – CJ shock, in the frame of the shock, was calculated to be 200 $\mathrm{m\,s^{-1}}$ using realistic thermal data. The laminar deflagration velocity is thus smaller than this gas speed by a factor of 7. Based on the significant difference between the required burning speed to keep up with the shock, and the burning velocity driven by diffusive phenomena, in a one dimension description of the shock-deflagration complex, diffusive effects would thus be negligible, as verified numerically by Singh, Leiberman & Shepherd (2003) and analysed in more detail by Clarke (1989). However, it is possible that the turbulization of the flame structure in multiple dimensions may provide an increase in the surface area of the flame in order to make the diffusive burning relevant to the structure and acceleration of the high-speed deflagration. For example, the numerical results in figure 21 show that the surface area of the unburned pockets is approximately two to four times the cross-section of the tube, and is increased by flow instabilities as the numerical resolution increases. Furthermore, according to the existing turbulent flame phenomenology (Damkohler 1940) and experimental results (Peters 2000), the turbulent burning velocity is given approximately by the magnitude of the velocity fluctuations in isotropic turbulence. This would thus require turbulent velocity fluctuations to be of the order of 200 $\mathrm{m\,s^{-1}}$. These are compatible with the large shears associated with the shock reflections (see figure 21). Future work should be devoted to resolving the problem of (turbulent) diffusive burning coupled with unsteady reactive gas dynamics.

6. Conclusions

The present study showed that the propagation and re-initiation of a detonation wave following the attenuation by one or several series of cylinders relies on shock reflections. Depending on the mixture sensitivity, one or several shock reflections may be necessary to re-amplify the attenuated detonation wave back to a self-sustained wave. The conditions for wave transmission found numerically were in good agreement with the experimental results. In the case of re-initiation following multiple shock reflections, a novel mechanism was identified, where each shock reflection gives rise to significant enhancement of the gas reactivity and burnout of large portions of unreacted gas. This leads to a slow acceleration of the leading front, punctuated by sudden re-accelerations. This acceleration mechanism, deduced from the numerical model, does not involve any diffusive phenomena. Nevertheless, calculations of the diffusive burning rates at conditions behind the transmitted shock of the experiments revealed that turbulent burning may locally contribute to the acceleration process provided large turbulent fluctuations are driven by the shock reflections. Future work should be devoted to the potential coupling of (turbulent) diffusive transport with compressible reactive hydrodynamics.

This work was supported by the NSERC Hydrogen Canada (H2CAN) Strategic Research Network Natural Sciences and Engineering Research Council of Canada (NSERC) through grant number 341897-07 to MIR and by the NSERC Hydrogen Canada (H2CAN) Strategic Research Network. B. McN. M. was also funded by an Ontario Graduate Scholarship. We wish to thank J. Lee for useful discussions and for permitting MIR to use the experimental facilities of his laboratory, supported by the Natural Sciences and Engineering Research Council of Canada (NSERC) through grant number A-3347. We would also like to acknowledge the help of A. Higgins and A. Yoshinaka for their original design of the experimental apparatus used in the present study and the assistance of J. Quirk with the AMRITA environment used for the numerical simulations.

REFERENCES

Akbar, R. 1997 Mach reflection of gaseous detonations. PhD dissertation, Rensselaer Polytechnic Institute, Troy, NY.

Arienti, M. & Shepherd, J. E. 2005 A numerical study of detonation diffraction. *J. Fluid Mech.* **529**, 117–146.

Austin, J. M. 2003 The role of instability in gaseous detonation. PhD dissertation, California Institute of Technology, Pasadena, CA.

Brailovsky, I. & Sivashinsky, G. 2000 Hydraulic resistance and multiplicity of detonation regimes. *Combust. Flame* **122**, 130–138.

Brailovsky, I. & Sivashinsky, G. 2002 Effects of momentum and heat losses on the multiplicity of detonation regimes. *Combust. Flame* **128**, 191–196.

Bykov, V., Goldfarb, I., Gol'dshtein, V., Kagan, L. & Sivashinsky, G. 2004 Effects of hydraulic resistance and heat losses on detonability and flammability limits. *Combust. Theor. Model.* **8**, 413–424.

Chao, J. C. 2006 Critical deflagration waves that lead to the onset of detonation. PhD dissertation, McGill University, Montreal, Canada.

Chao, J., Ng, H. D. & Lee, J. H. S. 2009 Detonability limits in thin annular channels. *Proc. Combust. Inst.* **32**, 2349–2354.

Clarke, J. F. 1989 Fast flames, waves and detonation. *Prog. Energy Combust. Sci.* **15**, 241–271.

Damkohler, G. 1940 The effect of turbulence on the combustion rate in gas compounds. *Z. Elektrochem. Angew. Phys. Chem.* **46**, 601–626.

Dionne, J.-P. 2000 Theoretical study of the propagation of non-ideal detonations. PhD dissertation, McGill University, Montreal, Canada.

Dionne, J. P., Ng, H. D. & Lee, J. H. S. 2000 Transient development of friction-induced low-velocity detonations. *Proc. Combust. Inst.* **28**, 645–651.

Dorofeev, S. B., Sidorov, V. P., Kuznetsov, M. S., Matsukov, I. D. & Alekseev, V. I. 2000 Effect of scale on the onset of detonations. *Shock Waves* **10**, 137–149.

Eckett, C. A., Quirk, J. J. & Shepherd, J. E. 2000 The role of unsteadiness in direct initiation of gaseous detonations. *J. Fluid Mech.* **421**, 147–183.

Frolov, S. M. 1987 Detonation in systems with friction, heat and mass transfer. PhD dissertation, University of Moscow, Moscow, USSR.

Gamezo, V. N., Ogawa, T. & Oran, E. S. 2008 Flame acceleration and DDT in channels with obstacles: effect of obstacle spacing. *Combust. Flame* **155**, 302–315.

Gamezo, V. N., Vasil'ev, A. A., Khokhlov, A. M. & Oran, E. S. 2000 Fine cellular structures produced by marginal detonations. *Proc. Combust. Inst.* **28**, 611–617.

Goodwin, D. 2010 CANTERA: an object-oriented software toolkit for chemical kinetics, thermodynamics, and transport processes. Available at: http://code.google.com/p/cantera/.

Gordon, S. & McBride, B. J. 1994 Computer program for calculation of complex chemical equilibrium compositions and applications. *Tech Rep.* 1311. NASA Reference Publication.

Gu, L. S. 1987 Effects of boundary conditions on the propagation of quasi-detonation waves. PhD dissertation, McGill University, Montreal, Canada.

Gu, L. S., Knystautas, R. & Lee, J. H. S. 1988 Influence of obstacle spacing on the propagation of quasi-detonations. In *Dynamics of Explosions; Progress in Astronautics and Aeronautics* (ed. A. L. Kuhl, J. R. Bowen, J.-C. Leyer & A. A. Borisov), vol. 114, pp. 232–247. American Institute of Aeronautics and Astronautics.

Ikeh, M. O. 1981 The passage of detonations through porous media. PhD dissertation, University of Michigan, Ann Arbour, MI.

Kauffman, C. W., Chuanjun, Y. & Nicholls, J. A. 1982 Gaseous detonations in porous media. In *Nineteenth Symposium (International) on Combustion.* The Combustion Institute, Pittsburgh, PA.

Khasainov, B., Presles, H. N., Desbordes, D., Demontis, P. & Vidal, P. 2005 Detonation diffraction from circular tubes to cones. *Shock Waves* **14**, 187–192.

Kiyanda, C. B. 2005 Photographic study of the structure of irregular detonation waves. Master's dissertation, McGill University, Montreal, Canada.

Knystautas, R., Lee, J. H. & Guirao, C. M. 1982 The critical tube diameter for detonation failure in hydrocarbon air mixtures. *Combust. Flame* **48**, 63–83.

Laney, C. B. 1998 *Computational Gasdynamics.* Cambridge University Press.

Lee, J. H. S. 2008 *The Detonation Phenomenon.* Cambridge University Press.

Lyamin, G. A., Mitrofanov, V. V., Pinaev, A. V. & Subbotin, V. A. 1991 Propagation of gas explosion in channels with uneven walls and in porous media. In *Dynamic Structure of Detonation in Gaseous and Dispersed Media* (ed. A. Borisov), vol. 153, pp. 51–75. Kluwer.

Mach, P. & Radulescu, M. I. 2010 Mach reflection bifurcations as a mechanism of cell multiplication in gaseous detonations. *Proc. Combust. Inst.* (in press). doi:10.1016/j.proci.2010.06.145.

Makris, A. 1993 The propagation of gaseous detonations in porous media. PhD dissertation, McGill University.

Makris, A., Papyrin, A., Kamel, M., Kilambi, J., Knystautas, R. & Lee, J. H. S. 1993 Mechanisms of detonation propagation in a porous medium. In *Dynamic Aspects of Detonation* (ed. A. L. Kuhl, J.-C. Leyer, A. A. Borisov & W. A. Sirignano), pp. 363–380. American Institute of Aeronautics and Astronautics.

Makris, A., Shafique, H., Lee, J. H. S. & Knystautas, R. 1995 Influence of mixture sensitivity and pore-size on detonation velocities in porous-media. *Shock Waves* **5**, 89–95.

Manzhalei, V. I. 1998 Gas detonation in a flat channel of 50 μm depth. *Combust. Explos. Shock Waves* **34**, 662–664.

Massa, L., Austin, J. M. & Jackson, T. L. 2007 Triple-point shear layers in gaseous detonation waves. *J. Fluid Mech.* **586**, 205–248.

Maxwell, B. M. 2010 One-dimensional model for predicting ignition during an accidental release of pressurized hydrogen into air. Master's Dissertation, University of Ottawa, Ottawa, Canada.

Obara, T., Sentanuhady, J., Tsukada, Y. & Ohyagi, S. 2008 Re-initiation process of detonation wave behind a slit-plate. *Shock Waves* **18**, 117–127.

Ohyagi, S., Obara, T., Hoshi, S., Cai, P. & Yoshihashi, T. 2002 Diffraction and re-initiation of detonations behind a backward-facing step. *Shock Waves* **12**, 221–226.

Peters, N. 2000 *Turbulent Combustion*. Cambridge University Press.

Pintgen, F. & Shepherd, J. E. 2009 Detonation diffraction in gases. *Combust. Flame* **156**, 665–677.

Quirk, J. J. 1998*a* AMR sol: design principles and practise. In *29th Computational Fluid Dynamics VKI Lecture Series, von Karman Institute* (ed. H. Deconinck). ISSN0337-8312; also available at www.amritacfd.org/cgi-bin/doc/vki.

Quirk, J. J. 1998*b* Amrita – a computational facility for CFD modelling. In *29th Computational Fluid Dynamics VKI Lecture Series, von Karman Institute* (ed. H. Deconinck). ISSN0337-8312; also available at www.amritacfd.org/cgi-bin/doc/vki.

Radulescu, M. I. 2003 The propagation and failure mechanism of gaseous detonations : experiments in porous-walled tubes. PhD dissertation, McGill University, Montreal, Canada.

Radulescu, M. I. & Lee, J. H. S. 2002 The failure mechanism of gaseous detonations: experiments in porous wall tubes. *Combust. Flame* **131**, 29–46.

Radulescu, M. I. & Maxwell, B. M. 2010 Critical ignition in rapidly expanding self-similar flows. *Phys. Fluids* **22**, 066101.

Radulescu, M. I., Papi, A., Quirk, J. J., Mach, P. & Maxwell, B. M. 2009 The origin of shock bifurcations in cellular detonations (CD-ROM). In Paper presented at the *22nd International Colloquium on the Dynamics of Explosions and Reactive Systems*, Minsk, Belarus, July 2009.

Radulescu, M. I., Sharpe, G. J., Law, C. K. & Lee, J. H. S. 2007 The hydrodynamic structure of unstable cellular detonations. *J. Fluid Mech.* **580**, 31–81.

Radulescu, M. I., Sharpe, G. J., Lee, J. H. S., Kiyanda, C. B., Higgins, A. J. & Hanson, R. K. 2005 The ignition mechanism in irregular structure gaseous detonations. *Proc. Combust. Inst.* **30**, 1859–1867.

Sharpe, G. J. 2001 Transverse waves in numerical simulations of cellular detonations. *J. Fluid Mech.* **447**, 31–51.

Singh, S., Leiberman, D. & Shepherd, J. E. 2003 Combustion behind shock waves. In *Western States Section/Combustion Institute*, Paper 03F-29, Pittsburgh, PA.

Slungaard, T., Engebretsen, T. & Sonju, O. K. 2003 The influence of detonation cell size and regularity on the propagation of gaseous detonations in granular materials. *Shock Waves* **12**, 301–308.

Sorin, R., Zitoun, R., Khasainov, B. & Desbordes, D. 2009 Detonation diffraction through different geometries. *Shock Waves* **19**, 11–23.

Teodorczyk, A., Lee, J. H. S. & Knystautas, K. 1988 Propagation mechanism of quasi-detonations. In *Twenty Second Symposium (International) on Combustion*. The Combustion Institute, Pittsburgh, PA.

Varatharajan, B. & Williams, F. A. 2001 Chemical-kinetic descriptions of high-temperature ignition and detonation of acetylene–oxygen-diluent systems. *Combust. Flame* **124**, 624–645.

Xu, S. J., Aslam, T. & Stewart, D. S. 1997 High resolution numerical simulation of ideal and non-ideal compressible reacting flows with embedded internal boundaries. *Combust. Theor. Model.* **1**, 113–142.

Zeldovich, Y. B., Gelfand, B. E., Kazhdan, Y. M. & Frolov, S. M. 1987 Detonation propagation in a rough tube taking account of deceleration and heat-transfer. *Combust. Explos. Shock Waves* **23**, 342–349.

Zeldovich, I. A. B. & Kompaneets, A. S. 1960 *Theory of Detonation*. Academic.

Zhang, F., Chue, R. S., Frost, D. L., Lee, J. H. S., Thibault, P. & Yee, C. 1995 Effects of area change and friction on detonation stability in supersonic ducts. *Proc. R. Soc. Lond.* A **449**, 31–49.

Zhang, F. & Lee, J. H. S. 1994 Friction-induced oscillatory behaviour of one-dimensional detonations. *Proc. R. Soc. Lond.* A **446**, 87–105.

Zhu, Y. J., Chao, J. & Lee, J. H. S. 2007 An experimental investigation of the propagation mechanism of critical deflagration waves that lead to the onset of detonation. *Proc. Combust. Inst.* **31**, 2455–2462.